Master of Science

University of Bergen
Department of Physics and Technology

Numerical Simulation of Laser Pulse Interaction With Circular Quantum Rydberg States of the Hydrogen Atom

Erik Flølo
Under the Supervision of Prof. Morten Førre

Submitted November 2021

Acknowledgements

The delivery of this thesis marks the end of my educational journey, and the five years I have spent at the university of Bergen. I am grateful for the free educational system provided by the Norwegian government, which is something many only can wish for. I also deeply want to thank my supervisor prof. Morten Førre, for all his good ideas and suggestions, and who set aside a great deal of time to provide feedback on this thesis. This could not have been done without you.

Abstract

The electron behaviour of the circular Rydberg state 5g(m=4) have been investigated under the influence of circularly polarized laser fields, by solving the Schrödinger equation numerically. Ionization dynamics were studied for fields that co- and counter-rotated the motion of the electron, and in both cases *atomic stabilization* were observed in a limited intensity regime. Angular distributions from both the co- and counter-rotating fields were found to be consistent with the single-photon selection rules given in [1]. Investigations were also performed using a field that rotated perpendicular to the plane of the 5g(m=4) electron distribution.

Contents

List of Figures

Atomic Units

For convenience, I will in this thesis mostly use *atomic units* when presenting numbers and equations related to quantum physics. A common name for this framework of units is *Hartree Atomic Units* (a.u.), where important constants such as m_e, $\hbar$, e and a_0 are all set to unity (= 1). When doing so, much of the mathematical formulations (such as the Schrödinger equation) takes on a much simpler form. The same goes for numbers involved in calculations, as they are simpler to work with and interpret. The SI-values for some of the most used units can be seen in the table below, and they are collected from the 2018 recommended data from *Committee on Data of the International Science Council* (CODATA) [2]. However, note that the displayed data have been rounded off to 4 significant digits.

Symbol	Measurement	Common Name	Definition	SI Value
a_0	Distance	Bohr Radius	$\frac{4\pi\epsilon_0\hbar^2}{(m_e e^2)}$	$5.292 \times 10^{-11} m$
$\hbar$	Action	Reduced Planck's Constant	$\frac{h}{2\pi}$	$1.055 \times 10^{-34} J \cdot s$
e	Charge	Fundamental Charge	e	$1.602 * 10^{-19} C$
m_e	Mass	Electron Mass	m_e	$9.109 * 10^{-31} Kg$
E_h	Energy	Hartre Energy	$\frac{\hbar^2}{m_e a_o^2}$	$4.360 * 10^{-18} J$

Chapter 1

Introduction

1.1 Background

It seem to be a very fundamental part of the human condition to explore unknown territories, to go one step further than what people in previous generations has been able to go before. Generation upon generation has contributed with new fundamental insights and discoveries to their field of study, and of course this applies to physics as well. There has been a rather steady advancement of new theoretical theories, but I believe many will agree with me when I say that the discovery of quantum mechanics and the wave-equation in the 1920's, turned out to be one of the most important ones for the field of physics [3].

Now in 2021, a wast amount of information on advanced topics such as Quantum Mechanics (QM) is just a click away. In previous generations however, it was only a selected few that got the training needed even to understand the slightest of physics, and so I consider myself lucky to be a master student in this day and age, where knowledge is available for those who seek it. With the recent fast development of the semiconductor-industry, the personal computer has become stronger than ever before. Even cheap laptops are now capable of performing simulations of complex atomic systems, that past philosophers of nature only could have dreamt of.

In fact, the main topic of this thesis will involve a numerical simulation of the interaction between a laser pulse and the electron in the hydrogen atom. Given that we have the theoretical and computational capabilities to perform such simulations, it is natural to ask what specific interactions we are interested in. When I start the discussion of the theoretical aspects around the laser interaction I will assume that that the reader of this thesis has a general background in physics, or at least is familiar with the outline of the most famous theories. Now, when reflecting on these simulations, there are many possible quantum states that the electron can exist in, and so we will be very interested in the changes these states go trough when interacting with the laser pulse. The first part will therefore contain a very brief introduction to atomic orbital theory, so that the reader can get an intuition on the geometry of the states we are interested in.

1.1.1 Atomic Orbitals

In introductory chemistry classes we quickly learn that the classical circular orbits predicted by the *Bohr model* is wrong, and that electrons orbit in very special

patterns called *atomic orbitals*. The shape of these orbitals are defined by a specific set of quantum numbers n, l and m originating from special requirements when solving the wave equation governing them. I will later go into some detail on solving this equation, but for now we should accept that these numbers are important and that they define the overall electron density shape. It is also well known that these orbitals often are labeled with letters s, p, d, e, f and g and so forth, instead of using the angular quantum number l. The shape for all orbitals having $l = 0$ (s) is simple and circular, but complexity quickly increase for larger values of l. This can bee seen in figure (1.1), where the real part of the *spherical harmonics* for the 5g (n=5, l=4) state is visualized. The red and blue colors correspond to different phases, but we are mostly concerned about the geometrical shape. If the z-axis is defined to be parallel to the longest dimension of the first 5g(m=0) state (upper left corner), then the state 5g(m=4) can be considered as a circular/torus shaped electron distribution, where the circular cross section is located in the xy plane, and can be seen in the bottom right corner of figure (1.1). However, these distributions must be interpreted with care. There has been published several articles on common misconceptions students have about orbitals, and in the article they usually state the importance of treating the orbitals only as approximations, especially within the field of chemistry where orbitals are frequently used [4].

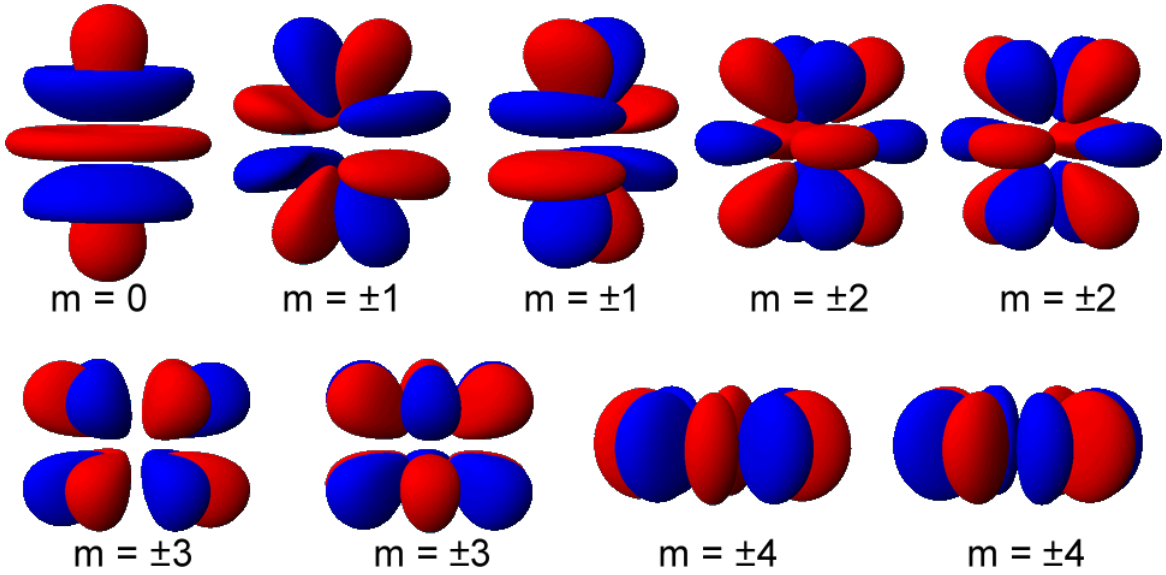

Figure 1.1: The 9 different 5g atomic orbitals, specified by the principle quantum number n = 5, the angular quantum number l = 4 and one value of the magnetic quantum number m. Note that the first circular orbital arrangement is observed for $m = \pm 4$. Later, this is referred to as the Rydberg state, 5g(m=4) or state $|544\rangle$. The orbitals are symmetrical for positive and negative values of m, and it therefore exists two identical versions with inverted phases (blue/red) related the sign of the wave function. Both signs are included for each orbital, since in reality it is a convention what sign one chooses to be a positive or negative phase. CopyRight-Certificate, and Source

The torus-shaped circular orbital from figure (1.1) labeled 5g(m=4), will be the main object of investigation in this thesis. As we will later see, this and similar states turn out to have very interesting properties. They are also a subcategory of

something called *Rydberg states*, which I will discuss in the next section.

1.1.2 Thesis Main Topic - Rydberg States

Rydberg atoms are highly excited atoms, where one of the valance electrons occupy a quantum state with a very large Principle Quantum Number (PQN) [5]. some of the important properties of these Rydberg states, comes from the fact that the expected distance the electron has from the nuclei, increase with the PQN. Therefore, since the singly excited valence electron in the Rydberg atom has a PQN that is much larger than many of the other electronic states, the average distance from the core will also be much larger. This will essentially mean that the exited electron feels the rest of the electrons as a combined coulombic potential originating from the core, and hence the system can closely resembles that of hydrogen [6]. The Rydberg atom have long been described in the scientific litterateur, without any significant scientific attention. In recent years this has changed, and Rydberg atoms now seem to be a hot topic within the physics community. For example, there has been published a collection of new articles on the topic of Rydberg atoms in a special issue from J. Phys. B, in 2017 [7]. One of the main reasons for the recent spike in scientific interest, comes from the potential usage of Rydberg atoms in different technologies, and especially quantum technologies [8]. A very important property being exploited for these technologies, is the sensitivity of these states to other adjacent Rydberg atoms and to small variations in the electric field (EF) [8]. For large PQN's the energy difference between neighboring quantum states are also very small (microwave), and this can be exploited to produce sensors for this domain of wavelengths. The sensitivity to other Rydberg atoms is often termed to be a result of the so called Rydberg Blockade [9]. The blockade effect can be explained in terms of the effective spatial expansion of an atom, accompanying its transformation into a Rydberg state. The accompanying expansion will shift and destabilize the energy levels of other close by atoms, resulting from the increased electron repulsion. If for example the photon energy is just enough to excite electrons to a specific energy level, then any upward shift in energy will prevent these electrons from reaching this state. An illustration of this *Rydberg Blockade* is given in figure (1.2). Here the left side shows three neighboring atoms, accompanied by an energy diagram for two adjacent atoms. The right side illustrates the effect of exciting the center atom to a Rydberg state, causing an upward shifts in the energy levels for the adjacent atoms, due to the increased electron repulsion. It must also be mentioned that there has been done experimental research on Rydberg atoms locally here at the University of Bergen. One of the topics investigated here was *intrashell dynamics* in Li-Rydberg atoms (n=25). In this research, internal transitions originating from Stark-Zeeman energy splitting, within the same n-shell was investigated. The Stark-Zeeman effects were induced by applying weak magnetic and electric fields. This resulted in a very small separation of internal energy levels, and therefore low-energy radio frequency photons were used as probes for these transitions [10]. Now, this was just some examples of why Rydberg states are interesting in general. I will now present a more specific subcategory of these states, namely circular Rydberg states.

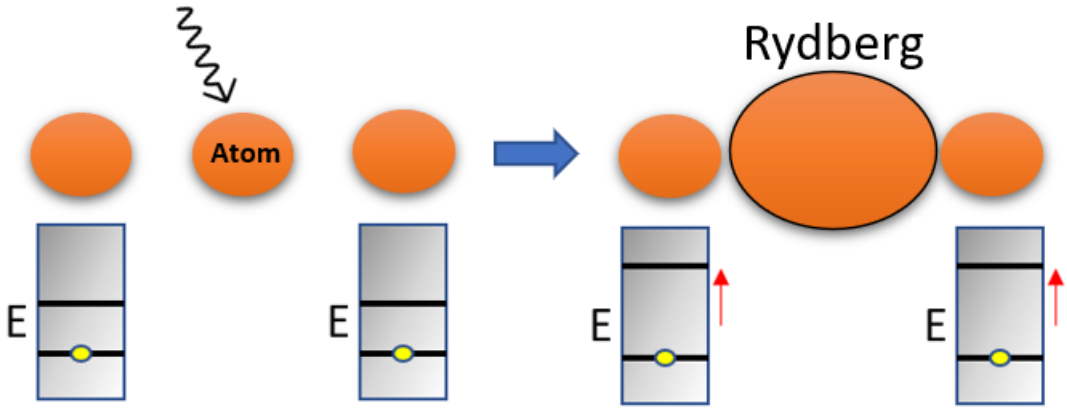

Figure 1.2: An illustration of the *Rydberg blockade*. The left side of the blue arrow shows the initial state before any excitation of the orange atoms. There is also displayed energy diagrams for the two atoms at the sides. The right side of the blue arrow, illustrates the effect of exciting the center atom into a Rydberg state, has on the energy levels. The adjacent atoms will experience an upward shift in higher energy levels, due to an effective increase in the electron repulsion. This is specified by the red upward-pointing arrows in the figure.

1.1.3 Circular Rydberg States

The circular Rydberg state is defined by having a large PQN, but also having a large value for the magnetic and angular quantum numbers, specifically where $m = l = |n-1|$ [11]. These circular states also turned out to be interesting for electromagnetic sensing technologies, and a recent publication in *Nature* presents the creation of a magnetic sensor, using an atom in a *superposition* between two circular Rydberg states [12]. As mentioned in the article, these circular states also have a long life expectancy (minutes) under certain conditions, making them suitable for interesting experimental procedures.

A new exciting theoretical framework was presented in a recent article (2017), where it was suggested to trap atoms in Rydberg states using laser physics [13]. The end goal was to perform quantum simulations of many body spin-systems, which have proven to be a very difficult task for the physics community to accomplish.

It must also be mentioned that circular Rydberg atoms have recently been a fundamental part in the research awarded the Nobel price in physics (2012) [14]. In this research, a special photon cavity (box) was created using two mirrors separated by 2.7cm and the circular Rydberg atoms with n = 50, 51 were used for their relative long life times as photon probes. In the experiments they managed to count, or measure individual photons by passing these circular atoms through this photon cavity. The measurement of individual photons is a truly remarkable accomplishment, illustrating the usefulness for researching these special states. The reader might now be interested in how it is possible to experimentally prepare atoms in these circular states in the first place. In the research performed at the University of Bergen, they prepared elliptical Rydberg states, as documented in [15]. I also included previously published material, containing a theoretical approach on how to prepare circular Rydberg states, here [16]. I have now given a few examples as to why these systems should be interesting to study, and illustrated that new theoretical insight in this

area could contribute to technological advancement in the future. The next section will cover an overview over the main objectives of this thesis, and the essence of the work that is to be done.

Thesis objective

The main objective that I want to accomplish in this thesis, is to perform an investigation of the electron behaviour in the circular Rydberg state 5g(m=4). The electron will be exposed to circular polarized light, originating from a simulated laser field. The electrons of the 5g(m=4) state rotates in a counter-clockwise manner, and I created a figure that illustrates the three different field orientations (red) that will be investigated, in relation to the electron motion (blue). The co-rotating field is illustrated in figure (3.1a), the counter-rotating field in figure (3.1b), and the field that rotates perpendicular to the xy-plane is illustrated in figure (1.3c), which is later referred to as the xz-polarized field. It will be of interest to see how some important measurable quantities change for these different field orientations. Some of these important quantities are ionization probabilities, kinetic energy distributions and angular distributions. I will look at how these quantities change over a range of field intensities, and compare some of my results to that of a previously published article.

I will now move over to cover more theoretical concepts necessary for the understanding of this work. I hope that I have managed to capture the readers attention, and that these systems seem meaningful to study, especially for their potential use in future technologies.

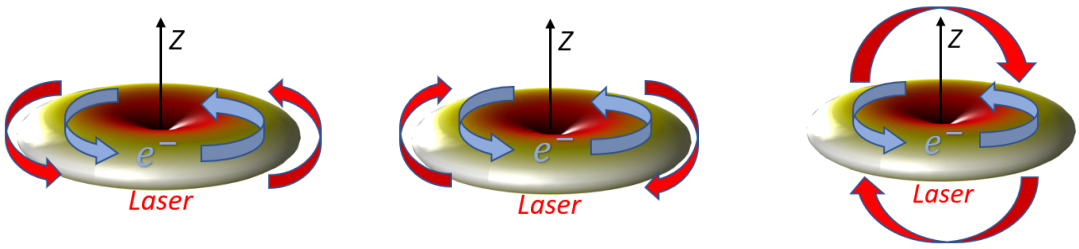

(a) Co-rotation (b) Counter-rotation (c) Perpendicular-rotation

Figure 1.3: The figure illustrates different orientations of the circular polarized laser pulse, in relation to the rotational motion of the electron distribution in the 5g(m=4) state. a) Illustrates a co-rotating pulse in the xy-plane. b) Illustrates a counter-rotating pulse in the xy-plane. c) Illustrates an xz-polarized pulse that rotates perpendicular to the xy-plane.

Chapter 2

Theory

As previously mentioned, the overall goal in this thesis is to perform a numerical simulation of the interaction between the electron in the hydrogen atom, and a polarized laser pulse. In order to do so, both the laser and the electron must be expressed in a suitable mathematical form. Electrons are governed by quantum mechanics, and so a brief overview on the basic concepts will be covered here.

2.1 Introduction to Quantum Mechanics

There are so many places one can start when introducing quantum mechanics, and different text books have different approaches. One such approach would be to start at the very beginning, including Max Planck's discovery of the *quanta*. In this section I will base much of the theory from a book used in some physics courses at UiB, and within the book I found a precise quote that I want to start this section with.

> "Quantum theory is based on two constructs: wave functions and operators" [17, p. 91].

In the end, this section can be summarised by two key components; the fact that we can express any system with wave functions, and that we can get information out from these wave functions by using some mathematical operations called *operators* on them. Now, let us have a look on some of the fundamentals of these wave functions.

2.1.1 Wave Functions

In quantum mechanics a particle like an electron, or system of particles are described by some wave function $\Psi(r, t)$. There has been a big debate around whether or not electrons really are particles or waves, since they show properties of being both under different type of measurements, like in the *double-slit experiment* [18]. For now, I will settle the debate by saying that electrons have both wave-like and particle-like properties, but cannot be classified as either of them.

A consequence of the wave-like behavior of particles is that the wave function describing the position of the particle is spread out in space. Therefore, calculating a precise location of the particle is not possible, like it is in classical mechanics. Nevertheless, we can calculate the probability for finding the particle between two

locations a and b, by integrating the absolute-square of the wave function between the two positions, see equation (2.1). This is a very important and widely known result, called *Born's statistical interpretation* [17, p. 4].

$$P_{ab}(a \leq x \leq b) = \int_a^b |\Psi(x)|^2 dx \tag{2.1}$$

The Born-relation is also tightly connected to something called *normalization*, where we demand that the integral over all possible values of $|\Psi(x)|^2$, should equal 1, as in equation (2.2).

$$\int_{-\infty}^{\infty} |\Psi(x)|^2 dx = 1 \tag{2.2}$$

In statistical terms, this is the equivalent requirement that the probability density-functions should integrate to 1 over their defined domains, and so the quantity $|\Psi(x)|^2$ should be interpreted as a probability density-function.

Now, I have introduced the first two *integrals* related to quantum mechanics, but they will not be the last. Integrals on the form of the *Dirac notation* $|\Psi\rangle$ (as will later be discussed) is one of the most common mathematical formulations we meet in QM. You will also see a lot of inner products between wave functions. This begs the question, since integrals are associated with functions, and inner products are associated with vectors, what will be the correct description of the wave function Ψ?

2.1.2 Hilbert Space

In quantum mechanics we express the wave functions in *Hilbert space* ($\mathcal{H}$), which is a vector space. This means that each wave function is built up by basis components from this space, and that we primarily use vector mathematics when working with these wave functions. We also know from basic linear algebra courses that matrices play a crucial role in the manipulation of vector spaces, which is also true when working in the Hilbert space.

As an example, if $|S(t)\rangle$ is a wave function defined on $\mathcal{H}$ containing a positional basis. Then we can extract the coefficient for the x-component $\psi_x(t)$, by taking the inner product between x and S, as shown in equation (2.3) [17, p. 114].

$$c_x(t) = \langle x|S(t)\rangle \tag{2.3}$$

And so, the total wave function $|S(t)\rangle$ is really represented as a vector, where the basis units can be functions as well. This is perhaps best illustrated by expressing the state as in equation (2.4).

$$|S(t)\rangle = \begin{pmatrix} c_x(t) \\ c_y(t) \\ c_z(t) \end{pmatrix} \tag{2.4}$$

Here the $c(t)$'s are time dependent coefficients, that express the relative occupation of the different eigenstates at any moment in time. Rest assured, the concept of eigenstates is something that will be discussed in a subsequent section.

To finish off, the answer to the question " if Ψ is a vector or a function?", is that it is essentially both. The wave function is represented as a vector where the unit

components are functions. Nevertheless, the wave function can be expressed by any set of basis functions, as long as they are a *complete set*, meaning they can span the whole Hilbert space. Just as an example, the unit vectors $\hat{x}$, $\hat{y}$ and $\hat{z}$ is a complete set for R^3. This means that any function part of the span of this space, can be represented as a linear combination of these basis functions. On the other hand, for the Hilbert space $\mathcal{H}$ the basis is the space of all square-integrable functions, on an interval that Ψ is defined on [17, p. 92]. There is an infinite number of such functions, and they can be complex, meaning that $\mathcal{H}$ can be represented by the complex space $\mathcal{C}^\infty$. Later, we will generate the wave functions numerically using a suitable basis, but for now it is enough to consider the wave function as a vector, where the basis components can be functions.

2.1.3 Basis Components of Psi

Now say that the quantum system $|S(t)\rangle$ is expressed in a basis of wave functions as we just mentioned, then we can also retrieve the components $c_n(t)$ from the n-th wave function $\psi_n(t)$ by taking the inner product with this basis function. This is expressed in equation (2.5).

$$c_n(t) = \langle n|S(t)\rangle \tag{2.5}$$

Note that a very common notation for the n-th wave function is $|n\rangle$. This is also known as the projection of the total wave function $|S(t)\rangle$, along that basis unit $\psi_n(t)$. Actually, the size of the projection coefficient squared, along a specific basis function $\psi_n(t)$, tells us how likely it is that the system will be measured in this state. In other words, the probability of measuring the wave function in state $|n\rangle$, can be expressed as equation (2.6).

$$P_n = |c_n(t)|^2 \tag{2.6}$$

After performing simulations, we would like to compute the probability for the electron to be torn away from the nuclei, known as the *ionization probability*. In order to compute this probability, we must take the squared-sum of all the coefficients corresponding to ionized states, and if N_{ion} is the number of such states, then the sum can be expressed as equation (2.7).

$$P_{ion} = \sum_{i=1}^{N_{Ion}} |c_i^{ion}(t)|^2 \tag{2.7}$$

In order to perform this sum, we must be able to differentiate between ionized and bound states.

2.1.4 Bound and Scattering States

In this thesis I will differentiate between two different type of eigenstates, based on their energy E. If the state has net-negative energy it is considered to be a *bound state*, while if it has net-positive energy it is considered as a scattered or ionized state. Since energy is a relative term, we can only make this generalization when assuming that the potential energy between the electron and the atomic core V(r), goes to zero at infinite distances [17, p. 63]. When using atomic units the potential

V(r) can be represented by equation (2.8), where r is the distance between the electron and the core.

$$V(r) = -\frac{1}{r} \tag{2.8}$$

Also, the brackets in (2.9) simplifies the distinction between the scattered and bound states.

$$\begin{cases} E & < 0 \implies \text{Bound State} \\ E & > 0 \implies \text{Scattered State} \end{cases} \tag{2.9}$$

So, going back to the formula for ionization probability in equation (2.7). The total ionization probability can now be found by summing together the individual probabilities from all the scattered states.

I will now move over to a slightly different topic, but which is still an essential concept of quantum mechanics, namely the quantum mechanical operators.

2.1.5 Hermitian Operators

One of the key concepts that has to be introduced when talking about quantum physics, is the quantum mechanical operator $\hat{o}$. The operator is a mathematical operation that works on the wave functions and retrieves some information from the system. In fact, the inner product with x that was previously introduced, is such an operator.

In quantum mechanics we are often left working with complex functions and values. However, in the end we usually want to calculate something that correspond to a real physical quantity. These real quantities are called **observables**, and their operators are called **Hermitian** [17, p. 95]. So what property does these Hermitian operators have?

First, We can find the expectation value of any observable as shown with *Dirac notation* in equation (2.10) [17, p. 94].

$$\langle \hat{Q} \rangle = \langle \psi | \hat{Q} \psi \rangle = \int \psi^\star \hat{Q} \psi dx \tag{2.10}$$

Since we now know that Hermitian operators return real values, this means the complex conjugate of the expectation value for $\hat{Q}$, has to be the same as shown in (2.11).

$$\langle \hat{Q} \rangle = \langle \hat{Q} \rangle^\star \tag{2.11}$$

This last constraint will allow us to reverse the operation order of $\hat{Q}$ since it is unchanged by complex conjugation, as in equation (2.12) [17, p. 94].

$$\langle \hat{Q} \psi | \psi \rangle = \langle \psi | \hat{Q} | \psi \rangle \tag{2.12}$$

.

Lastly, this has the final result that for any functions f and g we can swap the operation order according to equation (2.13) [17, p. 94]. This shows that any operator producing a real expectation value will do so for any general function, and must be *Hermitian*.

$$\langle \hat{Q} f | g \rangle = \langle \hat{Q} g | f \rangle \tag{2.13}$$

.

We now have some understanding of the mathematical operations that we will use on the wave functions to retrieve observables, but I have not yet introduced how to obtain the wave functions. Therefore, we must now discuss the equation that must be solved in order to find these functions in the first place, the Schrödinger equation.

2.1.6 The Schrödinger Equation

The Schrödinger equation (SE) is perhaps the most important equation in all of quantum mechanics, since this is the equation we must solve in order to find the wave functions $\Psi(x,t)$, which of course contains every information on the quantum-system we are working with. The Schrödinger equation can be seen seen in equation (2.14), where V is a potential [17, p. 25].

$$i\hbar \frac{\partial \Psi(x,t)}{\partial t} = -\frac{\hbar^2 \Psi(x,t)}{2m} + V\Psi(x,t) \tag{2.14}$$

Since time (t) is one of the variables in the equation, we are dealing with what is commonly called the *Time Dependent Schrödinger Equation*, or in short **TDSE**. In this section I will go through some of the important steps for solving this equation, and discuss some of the terminology introduced in introductory QM courses.

Those familiar with differential calculus, will recognize the TDSE as a second order partial differential equation, and so a common technique for solving these differential equations, is to perform *separation of variables*. This means that we can express Ψ as a product between one function depending only on position $\psi(x)$, and the other depending only on time $\varphi(t)$. There are some steps, but the important part is that we can put all the time dependent terms on one side, and x dependent terms on the other. Now, this last part is only possible assuming that the potential is time independent (e.g. Coulomb potential), then we can rewrite it as in equation (2.15) by introducing $\Psi(x,t) = \psi(x)\varphi(t)$ [17, p. 25].

$$i\hbar \frac{1}{\varphi}\frac{d\varphi}{dt} = -\frac{\hbar^2}{2m}\frac{1}{\psi}\frac{d^2\psi}{dx^2} + V \tag{2.15}$$

And so, since we have only time dependent terms on one side, and since this side should always equal the other containing only x-dependent terms, the consequence will be that both sides has to be equal to a constant E [17, p. 26]. This leaves us with two solvable differential equations in (2.16) and (2.17), where the solution to the time dependent part $\varphi(t)$ has been given.

$$-\frac{\hbar^2}{2m}\frac{d^2\psi}{dx^2} + V\psi = E\psi \tag{2.16}$$

$$\frac{d\varphi(t)}{dt} = -\frac{iE}{\hbar}\varphi(t) \;\rightarrow\; \varphi(t) = e^{-iEt/\hbar} \tag{2.17}$$

Lastly, the total energy of the system is encapsulated in the **Hamiltonian** operator $\hat{H}$ (2.18)

$$\hat{H} = -\frac{\hbar^2}{2m}\frac{\partial^2}{\partial x^2} + V \tag{2.18}$$

And so consequently, the *time independent* Schrödinger equation (TISE) can be rewritten in the short form as (2.19) [17, p. 27].

$$\hat{H}\psi = E\psi \tag{2.19}$$

This is known as an *eigenvalue* problem, where E is the eigenvalue for $\hat{H}$, and ψ the *eigenvector* or *eigenstate*. I will now discuss some of the fundamental aspects of these problems and how to solve them.

2.1.7 Eigenvalues and Eigenfunctions

Eigenvalue equations are frequently solved using linear algebra, and treated with matrices. We can follow the standard approach assuming the *Hamiltonian* is on matrix form. First rearranging equation (2.19) to (2.20).

$$\hat{H}\psi = E\psi \;\rightarrow\; (\hat{H}\psi - IE)\psi = 0 \tag{2.20}$$

If ψ consists of N eigenstates, then the *Hamiltonian* matrix transforms to equation (2.21).

$$\begin{pmatrix} H_{11} - E & . & . & . & H_{1N} \\ . & . & & & . \\ . & & H_{ii} - E & & . \\ . & & & . & . \\ H_{N1} & . & . & . & H_{NN} - E \end{pmatrix} \psi = 0 \tag{2.21}$$

This matrix problem correspond to N linear equations, that can be solved to find the correct eigenstates.

Given that $\hat{H}$ is in fact an **Hermitian** operator, then there exists a special theorem about the properties of the eigenfunctions of $\hat{H}$. The theorem states that "*Eigenfunctions beloning to distinct eigenvalues are orthogonal*" [17, p. 98]. This concept will be exploited later, since the eigenfunctions for the Hamiltonian will be used as a basis in our simulation, except that the dimension of ψ will be a lot larger than two. Also, since we are working with the hydrogen system, in principle we should find all the eigenstates of this system, corresponding to the ground state (1s) and subsequent excited states (2s, 2p, 3s .. 5g..). However, it will shortly be illustrated that due to our finite computational restrictions, the higher excited states will not be approximated close enough to resemble the analytical solutions, and will therefore be excluded from the simulation.

2.1.8 Schrödinger Equation - Spherical Coordinates

When representing the electron in hydrogen-like systems, where we can also assume that one-electron approximations hold (no electron-electron interactions), then the potential energy can often be expressed as a function of the electron's distance from the nucleus only. Therefore, in many cases it will be simpler to express the potential energy by one variable $V(r)$, instead of the three Cartesian points $V(x, y, z)$. With

this in mind, it looks to be very beneficial to express the Schrödinger equation in *spherical coordinates*. I will quickly go through some of the important steps when transforming it into the spherical coordinate system.

First, the Hamiltonian can be expressed as a sum of the kinetic and potential energy operators, as (2.22).

$$\hat{H} = \hat{T} + \hat{V} \tag{2.22}$$

We know from classical mechanics that kinetic energy can be expressed by momentum $T = \frac{1}{2m}p^2$, and so for 3 dimensions we have the result in (2.23) [17, p. 131].

$$\hat{H} = \frac{1}{2m}(\hat{p}_x^2 + \hat{p}_y^2 + \hat{p}_y^2) + V \tag{2.23}$$

Now, replacing the momentum operators with the quantum-mechanical short-version $\hat{p} = -i\hbar\nabla$, we have the form in (2.24).

$$\hat{H}\Psi(r,\theta,\varphi) = -\frac{\hbar}{2m}\nabla^2\Psi + V\Psi \tag{2.24}$$

In the transformation, the *Laplacian* operator (∇^2) will be transformed to the corresponding spherical coordinate version. Now, the solutions we are interested in, should be separable into a product between a radial $R(r)$ and an angular $Y(\theta,\varphi)$ function, as in equation (2.25).

$$\Psi(r,\theta,\varphi) = R(r)Y(\theta,\varphi) \tag{2.25}$$

This will lead to two equations, the ***Radial Equation*** (2.26) and the ***Angular Equation*** (2.27) [17, p. 134].

$$\frac{d}{dr}\left(r^2\frac{dR}{dr}\right) - \frac{2mr^2}{\hbar^2}[V-E]R = l(l+1)R \tag{2.26}$$

$$\left[\frac{1}{\sin\theta}\frac{\partial}{\partial\theta} - (sin\theta\frac{\partial Y}{\partial\theta}) + \frac{1}{\sin^2\theta}\frac{\partial^2}{\partial\varphi^2}\right] = -l(l+1)Y \tag{2.27}$$

Introducing the reduced radial wave function, $u(r) = rR(r)$ simplifies the radial equation into (2.28).

$$-\frac{\hbar^2}{2m}\frac{d^2u}{dr^2} + \left[V + \frac{\hbar^2}{2m}\frac{l(l+1)}{r^2}\right]u = Eu \tag{2.28}$$

Here the whole term enclosed in brackets is known as the *effective potential*, where you can see there is a positive/destabilizing contribution from the angular momentum quantum number l, which grows larger the closer the particle gets to the nucleus due to the r^2 term [17, p. 139]. For the hydrogen system, we replace V with the Coulomb potential, and by using *atomic units* the radial equation can be written as equation (2.29).

$$-\frac{1}{2}\frac{d^2u}{dr^2} + \left[-\frac{1}{r} + \frac{1}{2}\frac{l(l+1)}{r^2}\right]u = Eu \tag{2.29}$$

In this thesis, we are going to work with hydrogen-like systems, and so solving the radial equation in (2.29) will be important in order for us to find the reduced radial wave functions $u(r)$.

2.2 B Splines

2.2.1 Definition and Properties

B splines have been introduced in recent years as a very convenient way of representing the wave function. I refer the reader to the well cited article *Applications of B-splines in atomic and molecular physics* [19], which explains in more detail why the B-spline basis can compete with more traditional methods, such as *finite-difference*. Now, for the readers unfamiliar with the mathematical description of these splines, a short introduction that is highly based on the article I just mentioned, will be given. In this section, I will present the mathematical definition of the B splines, and introduce some of their properties.

B splines are piece wise polynomials of a certain degree k, having the recursive mathematical description seen in equation (2.30), and the very related definition for their derivative in equation (2.31) [19, p. 1823].

$$B_i^k(x) = \frac{x - t_i}{t_{i+k-1} - t_i} B_i^{k-1}(x) + \frac{t_i - x}{t_{i+k} - t_{i+1}} B_{i+1}^{k-1}(x) \tag{2.30}$$

$$\frac{dB_i^k(x)}{dx} = \frac{k-1}{t_{i+k-1} - t_i} B_i^{k-1}(x) - \frac{k-1}{t_{i+k} - t_{i+1}} B_{i+1}^{k-1}(x) \tag{2.31}$$

$B_i^k(x)$ is the numerical value of the $i'th$ spline of order k evaluated at x. Also having the following properties [19, p. 1823];

- t_j are knot-points and define the interval $I_i = [t_i, t_{i+1}]$, where only some specific B splines contribute $B_{i-k+1}, ...B_i$.
- They are normalized and complete so $\Sigma_i B_i(x) = 1$ over the larger knot-interval $[t_k, t_n]$.
- Base condition k = 1, is defined as $B_i^1(x) = 1$, when $x \in [t_i, t_{i+1}]$, otherwise $B_i^1(x) = 0$.
- $B_i^k(x)$ has *compact support* on $[t_i, t_{i+k}]$, meaning $B_i^k(x) = 0$, when $x \notin [t_i, t_{i+k}]$.
- B splines of order k ($B_i^k(x)$), are polynomials of degree k-1.

An important property of these splines, that we later want to exploit when constructing the Hamiltonian matrix, is that they can be integrated exactly over the knot interval they are defined on. The reason being that *Gauss Legendre integration (GL)* (2.32) is capable of integrating polynomials of a certain degree exactly.

$$\int_{-1}^{1} f(x)dx \approx \sum_{i=1}^{n} w_i f(x_i) \tag{2.32}$$

The necessary condition is that the polynomials that the integrated function f consists of, must be of degree 2n-1 or lower when the GL weights (w) are constructed using n points on each interval [19, 20]. Conveniently the degree we will get when constructing the matrix elements, are polynomials of degree 2k-2, since we are taking the product between two splines of order k, equivalent to the product between two polynomials of order k-1. Therefore, when performing the integration of these

functions, it is sufficient to use k number of points for each interval. So in general, the GL integration makes it possible to approximate an infinite sum (the integral), by only evaluating the polynomials at discrete points when introducing these GL weights.

However, as the attentive reader might have noticed, the GL quadrature in (2.32) poses a problem, since it is defined over the interval $x \in [-1, 1]$. The t-knots on the other side, are defined over our box limit $[0, r_{max}]$ and so what we actually want to do, is to integrate our polynomials on each such knot interval $x \in [t_i, t_i + 1]$. In order to do so, we use the corresponding transformation over to a general interval $[a, b]$, as shown in equation (2.33).

$$\int_a^b f(x)dx \approx \frac{b-a}{2} \sum_{i=1}^{n} w_i f\left(\frac{b-a}{2} x_i + \frac{a+b}{2}\right) \tag{2.33}$$

This method was implemented in the Python code to integrate the B splines that we used as basis for our wave functions.

2.2.2 B Splines as Basis for Wave Functions

The degree k of the B splines play an important role on the overall shape of the spline polynomials, and hence also its ability to represent a basis for wave functions. This can easily be seen when comparing B splines of different degrees with each other. A four-panel figure has been included in (2.1a)-(2.1d), where it is shown an ensemble of 4 different B splines with an increasing order of k, going left to right. Here it can be confirmed that the B splines having order k = 3 (2.1c) and k = 6 (2.1d) have a much closer resemblance with wave-like functions, than the splines of degree k = 1 (2.1a) and k = 2 (2.1b). A consequence of this, is that you can approximate the wave function with a set containing fewer B splines of higher-order, than the necessary number of lower-order B splines, to achieve the same numerical approximation. In fact, it is possible to approximate the wave functions using an order of k = 2, as long as we compensate with a sufficient number of B splines. The reason that k = 2 is the lowest possible order, is that the derivative of a k-order B-spline is defined recursively by using the B splines of order k-1. This means that the derivative would not be defined for k = 1, and so k = 2 is the lower bound.

Expressing the wave function with B splines therefore comes down to selecting a *sufficiently large* degree for k, in combination with a large enough number of B splines. An important note is that increasing the degree k, will not further improve the numerical accuracy when a certain precision has been reached. Since increasing the degree comes at the cost of computational time, it is desirable to choose the lowest possible value for k in combination with the number of B splines, without any significant loss in precision.

2.2.3 The Schrödinger Equation With B Splines

As has been previously mentioned, when solving the Schrödinger equation one uses a set of *complete* basis vectors to represent the wave function. Here we will use the B-spline functions as our initial basis to solve the eigenvalue equation as has been documented [19, p 1825]. I will denote the overall linear combination for a specified

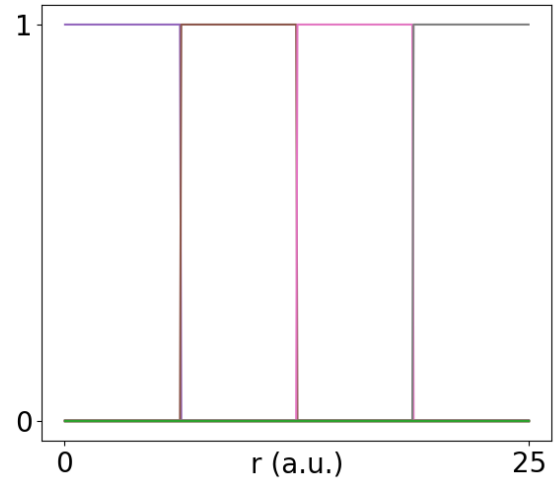

(a) B-spline order $\mathbf{k = 1}$.

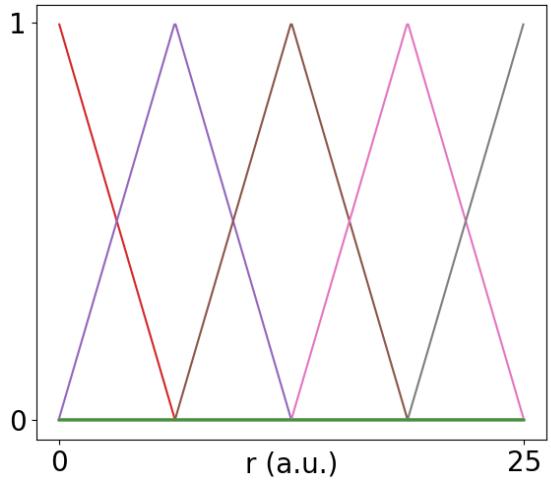

(b) B-spline order $\mathbf{k = 2}$.

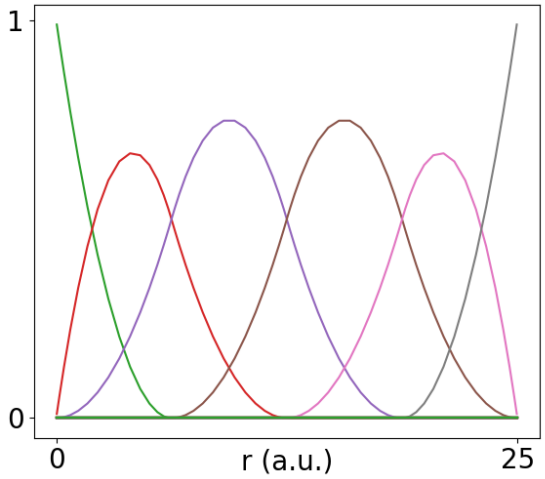

(c) B-spline order $\mathbf{k = 3}$.

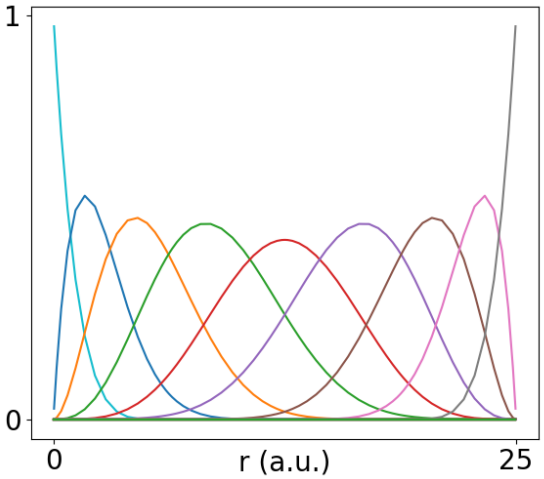

(d) B-spline order $\mathbf{k = 6}$.

Figure 2.1: Comparison between 4 sets of different B splines, having orders of k = 1, 2, 3 and 6 respectively. All of the above splines are plotted in the same radial box of 25 (a.u.), and all with 5 breakpoints each. The figure illustrates that increasing the order of k has a large effect for small values k = 1, 2, 3, but further increase from k = 3, to k = 6 is less significant on the overall shape of the B splines. Also note that there is a pair of B splines that does not converge towards 0 at the edge of each box, these were removed in order to enforce that the wave function should satisfy the boundary conditions.

radial wave function $u_{kl}(r)$ (2.34), referred to as a *core orbital* in [19].

$$u_{kl}(r) = \sum_{i=1}^{N^*} c_i^{kl} B_i(r) \tag{2.34}$$

The symbol k was chosen instead of the commonly encountered principle quantum number n, even if for some values they might be equivalent. However, for most

values they will not be related in this work. Also, note that the asterisk sign (N*) in the upper limit of the summation sign was included to separate it from another upper bound symbol N, that I will later use to limit the number of *core oribtals* included when calculating the matrix elements. This will be addressed in one of the following sections.

Finding the coefficients c_i^{kl}, belonging to a given $u_{kl}(r)$ state, is done by solving the Schrödinger equation. It will have a slightly different form, since the B splines are not orthogonal basis components. Nevertheless, they do span a complete basis and so any wave function can be expressed as a linear combination of them. The overlap matrix S will be included to take care of the non-orthogonality, and the resulting form of the *generalized eigenvalue problem* is seen in equation (2.35).

$$Hu_{kl}(r) = ESu_{kl}(r) \tag{2.35}$$

Where $u_{kl}(r)$ is a vector containing the corresponding coefficients with respect to the B-spline basis, as illustrated in (2.36).

$$u_{kl} = \begin{pmatrix} c_1^{kl} \\ c_2^{kl} \\ . \\ . \\ . \\ c_{N*}^{kl} \end{pmatrix} \tag{2.36}$$

The elements of the Hamiltonian matrix H_{ij} is calculated using the *reduced radial equation* (2.29) for hydrogen, as was discussed in the previous section. The specific mathematical expression for how the Hamiltonian elements H_{ij} are related to the B splines, is seen in equation (2.37), along with the definition for the elements of the overlap matrix S_{ij} in (2.38) [19, p. 1826]. Both of these expressions was implemented in Python.

$$\begin{aligned} H_{ij} = &-\frac{1}{2}\int_0^{r_{max}} B_i^k(r)\frac{d^2}{dr^2}B_j^k(r)dr + \frac{l(l+1)}{2}\int_0^{r_{max}}\frac{B_i(r)B_j(r)}{r^2}dr \\ &+ \int_0^{r_{max}} B_i^k(r)V(r)B_j^k(r) \end{aligned} \tag{2.37}$$

$$S_{ij} = \int_0^{r_{max}} B_i^k(r)B_j^k(r)dr \tag{2.38}$$

Now that we have H and S, the eigenvalue problem in (2.35) is something that is readily solved with the push of a button, in either *MATLAB* or *Python* using the *SciPy* library. We have now calculated our reduced radial wave functions $u_{kl}(r)$.

2.2.4 The Computational Box

In general we want to describe the wave functions as precisely as possible, in order to get the best computational results in our simulations. The problem is that when considering any radial wave function $R_{kl}(r)$, for some quantum state specified by k and l, it has a non-zero amplitude for all r. However, the radial wave functions decay

exponentially with distance for *bound states*, that is $R(r) \propto e^{-\lambda r}$, (see hydrogen radial WF (B.1)). This means that it might be enough for certain calculations to only include r values up to a certain maximum value r_{max}, where there would be little to no change in the calculation precision by increasing this value for r_{max}. That is, the results would essentially be the same, even if it would have been possible to simulate a box with infinite limits. An illustration can be seen in figure (2.2a), where three of the reduced radial wave functions $u_{kl}(r) = rR_{kl}(r)$ have been calculated for kl values matching the 1s, 2s and 3s states of hydrogen. The corresponding probability densities given by $[u_{kl}(r)]^2$, have been plotted in figure (2.2b). For those familiar with the shape of these wave functions, they look very similar to the analytical results. It is important to choose a sufficiently large box for the problem under investigation, so that the desired wave function can be represented accurately. For instance, the expected orbital distance for the electron $\langle r \rangle_n$ increases rapidly with the principle quantum number n. In fact it is proportional to the square for Rydberg states, that is $\langle r \rangle_n \propto n^2$ [5]. This means that even if we can model the ground state of hydrogen atom with a box having r_{max} of 25 atomic units (a.u.), we might fail to approximate excited states of higher energy (larger n). In this thesis we are going to simulate laser interactions with Rydberg states and these states are defined by their large values for n. To illustrate this problem, we can look at the wave functions we calculated in figures (2.2a) and (2.2b) and compare them to the exact analytical values. This can be seen in figure (2.3a), where a comparison between two different $u_{kl}(r)$ states has been performed. Here the calculated radial wave functions for the 2s and 3s states of hydrogen are plotted along with the exact analytical solutions. The plots are virtually identical for the 2s state shown in fig (2.3a), and so it seems that using box size of 25 (a.u.) is enough for this case. On the other hand, the radial probability plot for the 3s state seen in figure (2.3b) clearly shows that the analytical solution deviates from the calculated one. An important observation here, is that the analytical solution (3s) in yellow is actually hitting the edge of the right wall! This means that a box having r_{max} of 25 (a.u.), is not enough to approximate the wave function for the 3s state, and we would need to increase the size of the box, if we want a better approximation.

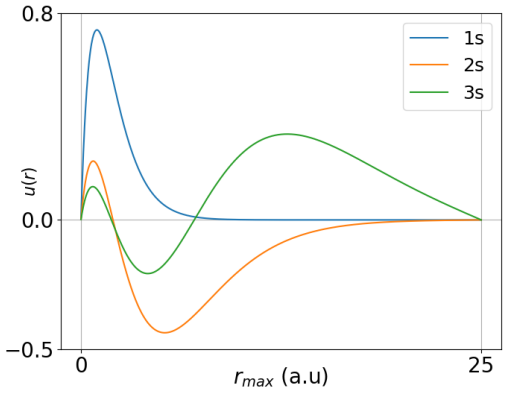

(a) Radial wave functions for 1s, 2s and 3s.

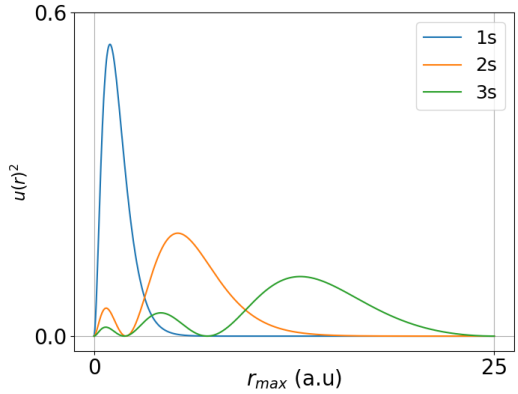

(b) Probability densities for 1s, 2s and 3s.

Figure 2.2: Radial and probability density plots for the 1s, 2s and 3s states of hydrogen. The reduced radial wave functions $u_{kl}(r) = rR_{kl}(r)$ are plotted using a box with radial dimension of $r_{max} = 25$ $(a.u.)$. B splines of order k = 5, and with a total number of $N_b = 100$ breakpoints were used when calculating the wave functions.

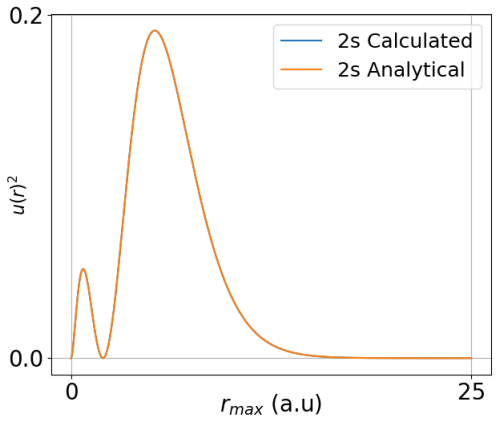

(a) 2s Radial probability density (match).

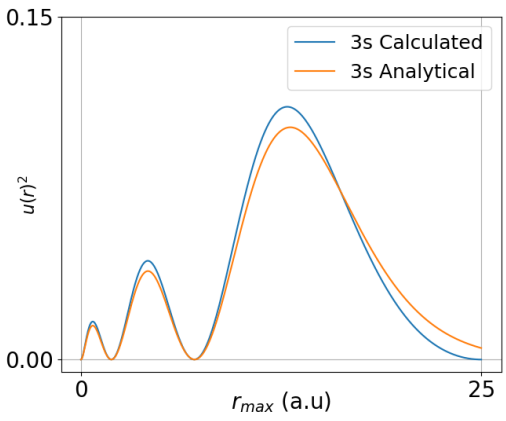

(b) 3s Radial probability density (miss).

Figure 2.3: Comparison between the calculated and analytical solution for probability density plots belonging to the 2s and 3s states of hydrogen. The box has a radial dimension of $r \in [0, 25a_0]$. The orange curve is the calculated result using B-splines as initial basis, while the blue curves are the exact analytical solutions. The plot illustrates that the box size of 25 (a.u.) is enough when computing the wave function for the 2s state (a), but not for the 3s state (b), where the density from the analytical wave function exceeds the box boundary.

Now that we have obtained wave functions describing the different electron states, we can move over to look at how the laser will effect the system, in *light-matter* interactions.

2.3 Laser Theory - Light Matter Interaction

In this section I will discuss the theory related to the light-matter interactions between the laser and the electrons. The laser has turned out to be one of the most important experimental equipment for most branches of physics during the last decades. It continues to be so, considering that parts of the 2018 Nobel prize in physics were awarded for work related to the production of high-intensity, ultra-short pulses [21]. In a recent publication researchers have used a femtosecond laser pulse to probe for ultra-fast electronic dynamics in nanomaterials (nanowires) [22]. The use of nanowires in combination with laser technology seem to be a hot research topic these days, exemplified by its recent use in experimental research at the *Lund Laser Center (LLC)* in 2021 [23]. Here a 10 TW laser was used for *laser driven proton acceleration*, illustrating yet another useful area. Lasers are *monochromatic* electromagnetic waves, so in order to understand lasers we need to have an understanding of electromagnetism.

2.3.1 Electromagnetism - Light

Electromagnetic waves (or light) are represented by two fields that oscillate orthogonal upon each other. These fields are known as the electric ($\vec{E}$) and magnetic ($\vec{B}$) fields. An illustration of light, represented by these fields in red and blue respectively, can be seen in figure (2.4).

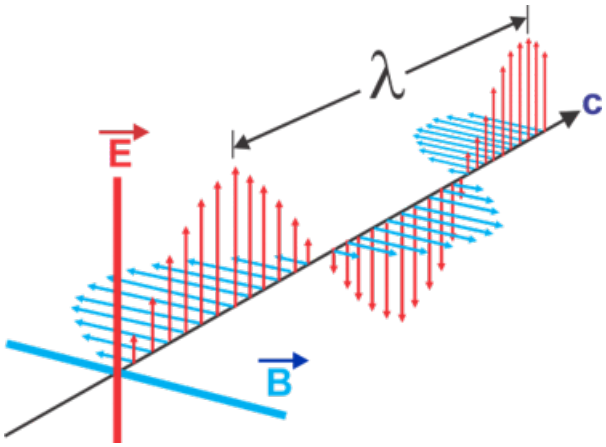

Figure 2.4: Illustration of the propagation of light. The light wave is composed of perpendicular oscillating electric ($\vec{E}$) and magnetic ($\vec{B}$) fields, that follow properties determined by Maxwell's equations. The wavelength λ determines the oscillation frequency, due to light moving at constant speed. Copyright License and image source

The oscillation frequency of light is related to its wavelength, as shown in equation (2.39).

$$\lambda = \frac{c}{f} \tag{2.39}$$

And the angular frequency is related the frequency as in equation (2.40).

$$\omega = 2\pi f \tag{2.40}$$

The properties of the electromagnetic wave is determined by Maxwell's equations seen in (2.41),

$$\begin{aligned} \nabla \cdot \vec{E} &= \frac{\rho}{\epsilon_0} \\ \nabla \times \vec{E} &= -\frac{\partial \vec{B}}{\partial t} \\ \nabla \cdot \vec{B} &= 0 \\ \nabla \times \vec{B} &= \mu_0 \vec{J} + \mu_0 \epsilon_0 \frac{\partial \vec{E}}{\partial t} \end{aligned} \tag{2.41}$$

where ρ is the electric charge density, $\vec{J}$ the current density vector and ϵ_0, μ_0 are the vacuum constants of *permittivity* and *permeability* respectively. The four equations in (2.41), are the compact differential form of the original set of 20 equations that Maxwell presented in his article on electromagnetism in 1864 [24]. They all have common names, which is from top to bottom, *Gauss's law*, *Faraday's law*, *Gauss's law for magnetic fields* and *Ampere's law*. The equations shown in (2.42) and (2.43) represent the E- and B-field when the electromagnetic wave is propagating along the x-axis. Here the E-field will oscillate in the z-plane, and the B-field in the y-plane.

$$\vec{E}(x,t) = E_0 sin(kx + \omega t)\hat{z} \tag{2.42}$$

$$\vec{B}(x,t) = B_0 sin(kx + \omega t)\hat{y} \tag{2.43}$$

Both waves are described by the amplitude components E_0 and B_0, multiplied by the oscillating sine-term. The direction of the fields are determined by multiplication along a unit vector $\hat{z}$ and $\hat{y}$. Also, since the electric field only propagates along a single dimension, we are dealing with a type of *linear polarization*. This is in contrast to the *circular polarized* electromagnetic fields, which contain two electric field components, which will be further discussed later. In the next section I will discuss the dipole approximation, which will simplify the modeling of the electromagnetic interactions.

2.3.2 Dipole Approximation

In laser physics you frequently encounter papers that mention the so called *dipole approximation* [25, 1, 26]. The essence of this approximation comes from having an electromagnetic field that has a much larger wavelength than the system being illuminated, as for example the hydrogen atom and a near infrared 800 nm laser. Here the electric field strength will be spatially independent, and only depend on time. Also, the magnetic field strength is related to the electric field strength by $|\vec{B}| = |\vec{E}|/c$, where c is the speed of light. Since c is very large, the magnetic field can be neglected for all electric field strengths investigated in this thesis. The concept of the *dipole approximation* is illustrated in figure (2.5), where two hydrogen atoms are

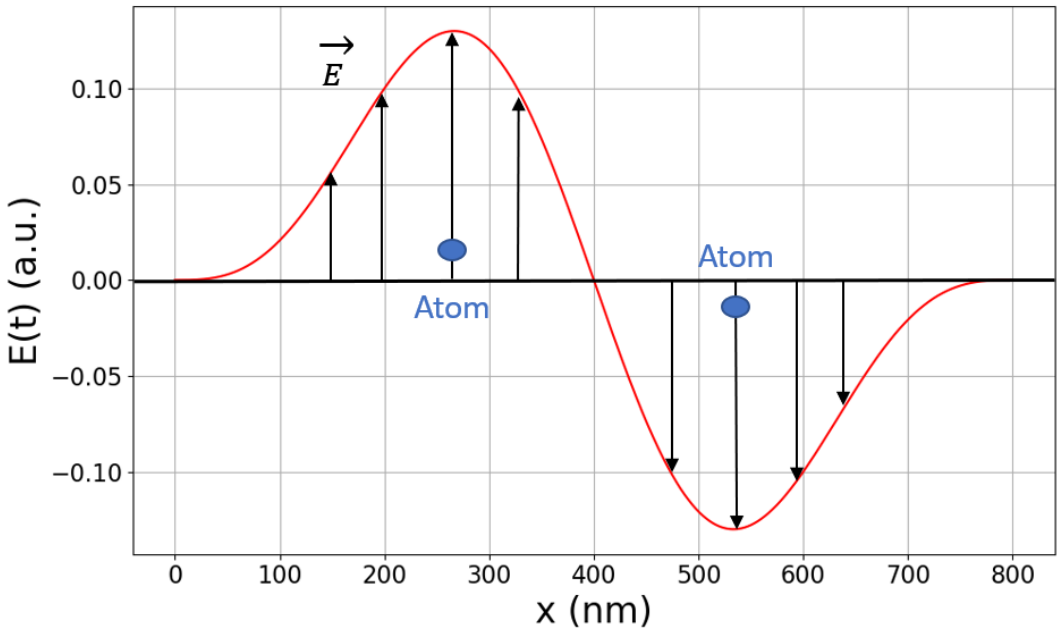

Figure 2.5: The figure illustrates why the dipole approximation can be considered accurate when using a red laser, having a wavelength of $\lambda = 800\ nm$. Each hydrogen atom will be much smaller than the wavelength of the laser, which means they will feel the same electric field strength at a given moment in time, therefore field interactions are independent of position.

represented by blue dots within the laser pulse. Due to each atom being much smaller than the wavelength of the laser, they experience the same electrical force from the E-field, which is here represented by black arrows. However, in high-intensity fields the dipole approximation might break down. Nevertheless, with lasers close to the 800 nm wavelength regime, the dipole approximation is considered to be valid for intensities below $5 \times 10^{15}\ W/cm^2$ [26]. In this thesis every simulation will be performed below the breakdown region just mentioned, so the dipole approximation has been assumed to hold. I will now further discuss the representations of linear and circular polarized fields.

2.3.3 Field Polarization

The direction of polarization is determined by the electric field components. If the electric field oscillate in a single dimension it is a form of *linear polarization*, but in this thesis I will only use *circular polarization* of the electric field. The *circular polarization* is created by including field components in two orthogonal directions with a relative phase shift between them.

The laser in this thesis will be described in terms of the *vector potential* $\vec{A}$, which is related to the electric field ($\vec{E}$) and magnetic field ($\vec{B}$) as shown in equation (2.44) and (2.45).

$$\vec{E} = -\frac{\partial \vec{A}}{\partial t} \tag{2.44}$$

$$\vec{B} = \vec{\nabla} \times \vec{A} = 0 \tag{2.45}$$

Here equation (2.45) must equal zero if the magnetic field is to be neglected. A suitable representation for the laser that satisfy both of the above equations, and is expressed in terms of the *vector potential* $\vec{A}$, is given in equation (2.46),

$$\vec{A}_p(t) = A_0 \sin^2(\frac{\pi t}{T}) \sin(\omega t + \varphi_j)\hat{u_p} \tag{2.46}$$

where we have that $A_0 = E_0/\omega$, and ω being the oscillation frequency of the laser [1]. E_0 being the maximum electric field amplitude, and T is the pulse duration. The direction of polarization will be along the unit vector $\hat{u_p}$, and the symbol φ_j is the *carrier envelope phase* or *CEP*, which is the relative phase difference between the carrier and envelope wave. The number of cycles (N_c) the laser goes through is related to the total time T and the frequency ω of the laser as in equation (2.47).

$$T = (N_c) \times \frac{2\pi}{\omega} \tag{2.47}$$

Also, the *CEP* term can be modified to function as the phase difference between the components in the circular polarized field, which I will discuss in the next section.

2.3.4 Representation - Circular Polarization

A circular polarized field having a clockwise rotation was created by setting the CEPs $\varphi_x = 0$ and $\varphi_y = \pi/2$. The respective expressions for the laser in the x, and y dimensions, then becomes as equation (2.48) and (2.49).

$$\vec{A}_x(t) = A_0 \sin^2(\frac{\pi t}{T}) \sin(\omega t + \varphi_x)\hat{i} \tag{2.48}$$

$$\vec{A}_y(t) = A_0 \sin^2(\frac{\pi t}{T}) \sin(\omega t + \varphi_y)\hat{j} \tag{2.49}$$

The direction of rotation can easily be reversed to a counter-clockwise field by interchanging the phase difference, setting $\varphi_x = \pi/2$ and $\varphi_y = 0$. For positive m-values the rotational term in the wave function $e^{im\varphi}$, rotates in a counter-clockwise manner. This means that the field that co-rotates with the electron motion is the counter-clockwise rotating field, while the clockwise-rotating field will be counter-rotating the motion of the electron.

I have now presented the mathematical representations of the linear and circular polarized pulses, but in order to get an intuitive understanding of the pulse dynamics, it might be useful to visualize the amplitude variations of the laser pulse through time.

2.3.5 Pulse Visualization

The change in amplitude of the laser pulse through time can be illustrated by plotting the mathematical representation shown in equation (2.46), by choosing a set of values for the different parameters discussed in the previous section T, ω, E_0 and φ. The result for one such plot can be seen in figure (2.6), having the set of parameters $E_0 = 10$ (a.u.), $\omega = 50$ (a.u.), $N_c = 15$, $\varphi = 0$.

The pulse in figure (2.6) illustrates how the intensity of this linear polarized field evolves through time, and shows that it has the characteristic form of a *wave-packet*.

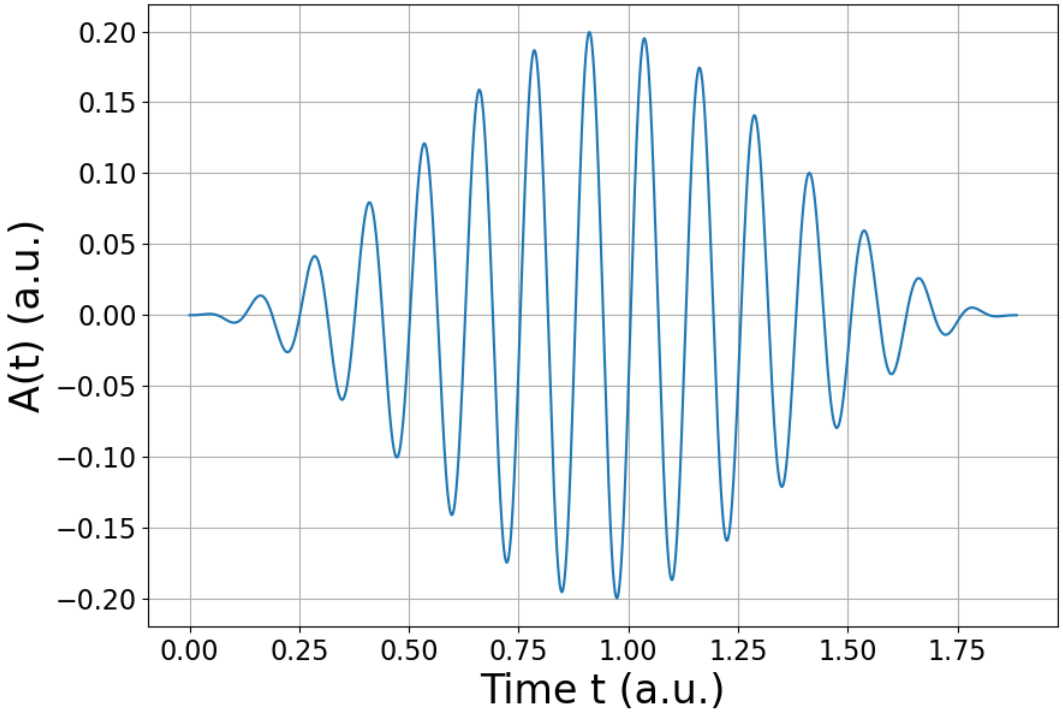

Figure 2.6: Visualization of the change in amplitude through time for a linear polarized 15-cycle laser pulse, determined by equation (2.46). The parameters for the pulse are $E_0 = 10$ (a.u.), $\varphi = 0$ and $\omega = 50$ (a.u.).

The laser amplitude is limited by the sine-squared term, and so it functions as an envelope for the upper and lower bounds.

I have also included a two-panel figure that illustrates the difference in geometry between a 4-cycle pulse in figure (2.7a) and a 12-cycle pulse in figure (2.7b), having identical frequency and phase. Simulations using low-cycle pulses as the 4-cycle case, will have a much smaller total simulation time compared to the many-cycle pulses. This means that many-cycle pulses are more computational expensive to simulate.

In the next section, I will demonstrate how the amplitude evolves through time for the circular polarized fields.

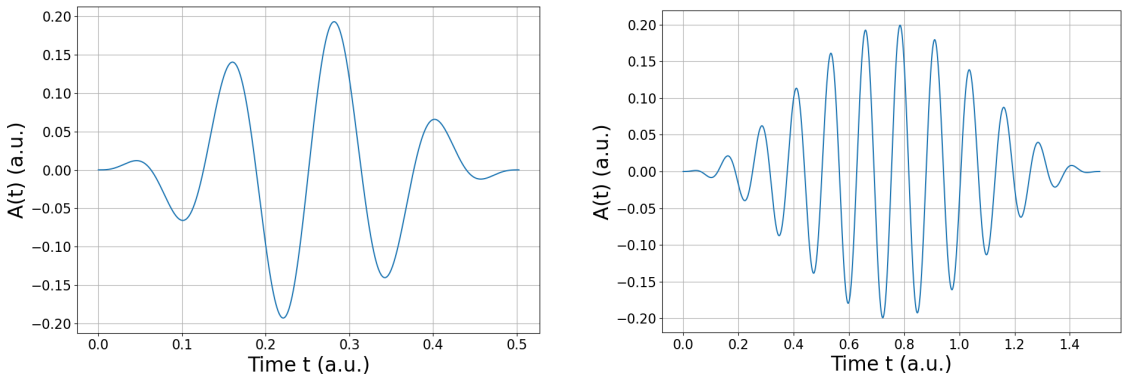

(a) 4-cycle laser pulse.

(b) 12-cycle laser pulse.

Figure 2.7: Comparison between a 4-cycle (a) and a 12-cycle (b) laser pulse. Each pulse duration was chosen according to the formula $\mathrm{T} = N_c \frac{2\pi}{\omega}$, in order to complete the 4 and 12 cycles. The laser intensity was set to $E_0 = 10$ (a.u.), using a *CEP* of $\varphi = 0$ and frequency $\omega = 50$ (a.u.). The laser amplitude $A(t)$ was calculated using equation (2.46).

Visualization - Circular Polarization

In the previous section, I visualized how the amplitude of a linear polarized pulse behave over the full pulse duration. Since rotating fields are essential to the project of this thesis, I also want to visualize how the geometry of these pulses change through time. It is also of interest to see how the relative amplitudes of each component change with respect to rotation of the field, and so I plotted the x and y components of a 4-cycle $\omega = 50$ (a.u.) field for the full pulse duration, as seen in figure (2.8). Here the rotation is in the xy-plane, and the components of the laser $A_x(t), A_y(t)$ are determined by the mathematical expressions for the clockwise rotation, previously given in equation (2.48) and (2.49). In order to illustrate the direction of rotation, I plotted 50 vectors with an even spacing in time for the first third of a full pulse duration. It can be seen from the figure that the vectors rotate in a clockwise manner, if it is known that they started from the origin. It can also be seen that the vectors goes through a symmetrical cycle, ending up in the same position that they started from.

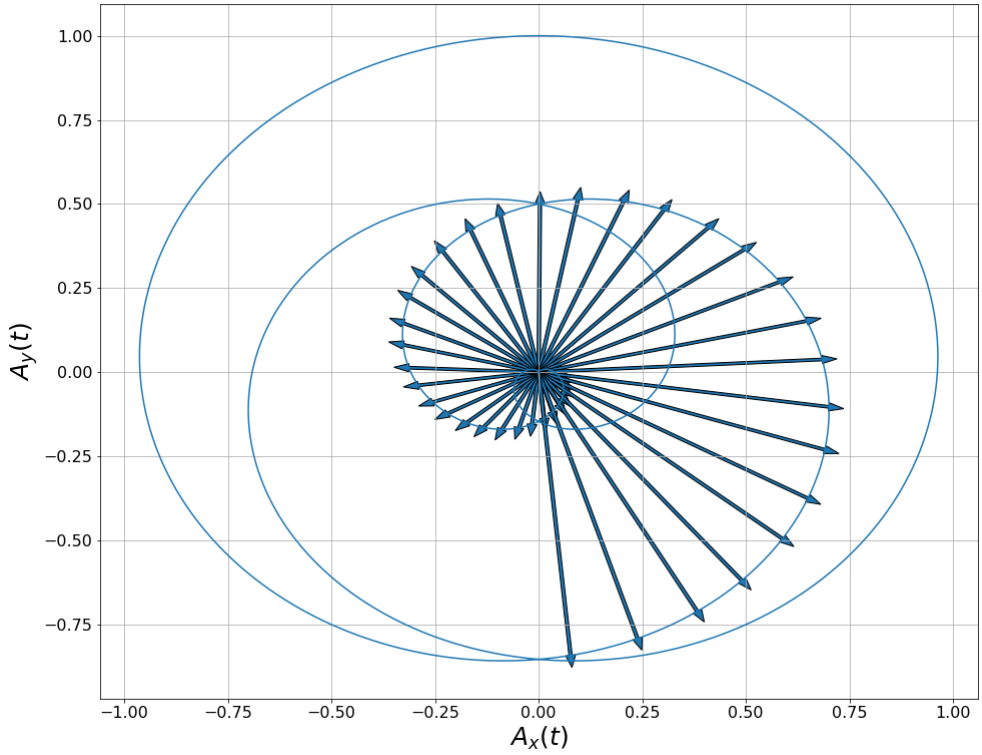

Figure 2.8: Illustration of the circular polarized field at every point in time for a 4-cycle pulse, having $\omega = 50$ (a.u.). Each point is determined by the components $(A_x(t), A_y(t))$, at a given point in time. The direction of rotation is visualized by plotting 50 vectors for the first third of the full simulation time T, expressed as the combination $\vec{A}(t) = \vec{A}_x(t) + \vec{A}_y(t)$.

The next section covers how the light-matter interaction between the laser and electron will be included in the Hamiltonian.

2.3.6 Minimal Coupling Hamiltonian

When the electric field is the only contributing field component, the form of the *minimal-coupling* Hamiltonian H can be written as equation (2.50).

$$H = \frac{1}{2m}[\vec{p} - qA(\vec{t})]^2 + V \tag{2.50}$$

This minimal-coupling is also commonly referred to as the *velocity-gauge Hamiltonian*, and a more comprehensive discussion on this concept and beyond the dipole approximation can be read here [27].

The minimal-coupling Hamiltonian belongs to a particle in a Coulomb potential V, having mass m and charge q. $\vec{A}$ is known as the *vector potential*, which has previously been related to the electric field in equation (2.44). In classical electromagnetism the *Lorentz Force* shown in equation (2.51), is the force acting upon an electron with velocity v, moving through an electric field $(\vec{E})$ and magnetic field $(\vec{B})$. In order to include this force in the Hamiltonian, it must be expressed in terms of the *vector potential* $\vec{A}$. The reason being that it cannot be expressed as a scalar potential-energy function under the formulation given in equation (2.51) [17, p. 181].

$$\vec{F} = q(\vec{E} + \vec{v} \times \vec{B}) \tag{2.51}$$

When the terms in the *minimal-coupling* Hamiltonian are expanded out completely, it transforms to equation (2.52).

$$H = \frac{(\vec{p})^2}{2m} + V - \frac{q}{m}\vec{A} \cdot \vec{p} + \frac{q^2}{2m}(\vec{A})^2 \tag{2.52}$$

The last term containing $(\vec{A})^2$ can be neglected under the dipole approximation, but is known to contribute in beyond-dipole effects, as in super-intense laser fields [25]. This reduces the Hamiltonian to equation (2.53).

$$H = \frac{(\vec{p})^2}{2m} + V - \frac{q}{m}\vec{A} \cdot \vec{p} \tag{2.53}$$

Using atomic units, we can rewrite it as equation (2.54), assuming the laser has polarization in all of the spatial directions x, y and z.

$$H = \frac{(\vec{p})^2}{2} - \frac{1}{r} + A_x p_x + A_y p_y + A_z p_z \tag{2.54}$$

We now have all the necessary theoretical concepts in place, to generate the *minimal coupling* Hamiltonian matrix, which will be the topic of the next section.

2.4 Generating Matrix Elements

In this section I will introduce how the elements of the *minimal-coupling* Hamiltonian are generated, by using the previously established theoretical concepts. Each matrix element is generated by using the minimal-coupling Hamiltonian between two states of the system, as shown in equation (2.55).

$$\langle \psi_{klm}(r,\theta,\varphi)|H|\psi_{k'l'm'}(r,\theta,\varphi)\rangle = \langle \frac{u_{kl}(r)}{r} Y_l^m(\theta,\varphi)|\, H \,|\frac{u_{k'l'}(r)}{r} Y_{l'}^{m'}(\theta,\varphi)\rangle \tag{2.55}$$

Here the wave function $\psi_{klm}(r,\theta,\varphi)$ has been expanded in terms of the reduced radial wave functions $u_{kl}(r)$, and the corresponding spherical harmonics $Y_l^m(\theta,\varphi)$. As mentioned, the radial functions were found by previously solving the time independent radial equation, using B-splines as basis functions. The Hamiltonian here is the version from equation (2.54), which was discussed in the previous section. Since the basis functions correspond to quantum states specified by k, l and m we can specify the general matrix element with a shorter notation, shown in (2.56).

$$\langle klm|\, H \,|k'l'm'\rangle \tag{2.56}$$

The matrix element generation has now been reduced to a loop over all possible state combinations, which was implemented in Python. In principle, there is an infinite amount of eigenstates, however many of the states having large energies will most likely be poor approximations. Therefore, we will truncate the number of total states from each l-channel, and only compute the interaction between the first N states. The value for N is then determined by setting a maximum energy E_{max}, so that no state has an energy that exceeds this limit.

This means that for a specific lm-combination we have a total of $N \times N$ matrix elements, where each element will be assigned a left index (i) and right index (j). These indexes will then be used to represent the Hamiltonian on matrix form H_{ij}, which will be discussed in more detail shortly. The total number of lm-combinations can be limited by setting an upper bound for l (l_{max}), in which the value for m will also be limited according to the well know restriction rule in (2.57).

$$m \in [-l, l] \tag{2.57}$$

The problem size grows rapidly with l_{max}, due to the $N \times N$ element generation for each unique lm-pair. The total number of pairs can be counted by considering the restriction rule for m, which leads to a sum over m from -l to l for each l-value. The total amount of m states will therefore be 1, 3, 5.. for l = 0, 1, 2.., and so forth. This means that the total number of pairs can be expressed as the double summation in equation (2.58), which conveniently turns out to be the sum of the first $l_{max}+1$ odd numbers, having a short and precise mathematical expression.

$$lm_{pairs} = \sum_{l=0}^{l_{max}} \sum_{m=-l}^{l} = 1 + 3 + 5 + 7.. = (l_{max} + 1)^2 \tag{2.58}$$

Many of the matrix elements turn out to be zero, and it would be very convenient to skip the evaluation of these integrals. There exist what is known as *selection rules* for the quantum numbers l and m, allowing us to identify all non-zero elements [17, p. 420]. These selection rules are unique for each of the p_x, p_y and p_z momentum terms, which can be seen in equation (2.59).

$$\begin{aligned} p_x &: \Delta l = \pm 1, \Delta m = \pm 1 \\ p_y &: \Delta l = \pm 1, \Delta m = \pm 1 \\ p_z &: \Delta l = \pm 1, \ \Delta m = 0 \end{aligned} \tag{2.59}$$

These selection rules were implemented, so that only non-zero integrals were computed. I will demonstrate the origin of the p_y selection rule, when deriving the $A_y(t)p_y$ coupling element shortly. There are three terms we are interested in, one for each of the directions in $\vec{A} \cdot \vec{p}$, that contains p_x, p_y and p_z respectively. All three terms can be seen in equation (2.60).

$$\langle klm|A_x \cdot \hat{p_x}|k'l'm'\rangle + \langle klm|A_y \cdot \hat{p_y}|k'l'm'\rangle + \langle klm|A_z \cdot \hat{p_z}|k'l'm'\rangle \tag{2.60}$$

In the next section, I will go through the derivation of the p_y-elements.

2.4.1 Deriving p_y - Elements

The momentum operator $\hat{p_y}$ is defined as $\hat{p_y} = -i\frac{\partial}{\partial y}$ when using *atomic units*, and involves the derivative expressed in the Cartesian system. However, since we have expressed our wave functions in spherical coordinates using $u_{kl}(r)$ and $Y_l^m(\theta, \varphi)$, then we must also express d/dy in spherical coordinates. There is also the contribution from the vector potential A_y. However, this contribution is just a time dependent scalar under the *dipole approximation*, and can be moved outside the integral. If we only consider the y-dimension, we are left with equation (2.61).

$$\langle klm|A_y \cdot \hat{p_y}|k^{'}l^{'}m^{'}\rangle = A_y\langle\frac{u_{kl}(r)}{r}Y_l^m(\theta,\varphi)| - i\frac{\partial}{\partial y}|\frac{u_{k^{'}l^{'}}(r)}{r}Y_{l^{'}}^{m^{'}}(\theta,\varphi)\rangle \tag{2.61}$$

In spherical coordinates, we have that $\partial/\partial y$ can be represented as (2.62).

$$\frac{\partial}{\partial y} = \sin(\theta)\sin(\phi)\frac{\partial}{\partial r} + \frac{1}{r}\sin(\phi)\cos(\theta)\frac{\partial}{\partial\theta} + \frac{1}{r}\frac{\cos(\phi)}{\sin(\theta)}\frac{\partial}{\partial\phi} \tag{2.62}$$

So the full expression can now be written out as (2.63)

$$-iA_y\langle\frac{u_{kl}(r)}{r}Y_l^m(\theta,\varphi)|\sin(\theta)\sin(\phi)\frac{\partial}{\partial r}+\frac{1}{r}\sin(\phi)\cos(\theta)\frac{\partial}{\partial\theta}+\frac{1}{r}\frac{\cos(\phi)}{\sin(\theta)}\frac{\partial}{\partial\phi}|\frac{u_{k^{'}l^{'}}(r)}{r}Y_{l^{'}}^{m^{'}}(\theta,\varphi)\rangle \tag{2.63}$$

The full derivation of this expression can be read in Appendix (A.1), but the important and final result for the p_y matrix elements are shown in (2.64).

$$\begin{aligned}
&-i\langle\frac{u_{kl}(r)}{r}Y_l^m(\theta,\varphi)|\frac{\partial}{\partial y}|\frac{u_{k^{'}l^{'}}(r)}{r}Y_{l^{'}}^{m^{'}}(\theta,\varphi)\rangle = \\
&-a_{l,-m}\delta_{l,l-1}\delta_{m,m+1}\int_0^{r_{max}} u_{kl}\left(\frac{du_{k^{'},l-1}}{dr} - \frac{l}{r}u_{k^{'},l-1}\right)dr \\
&-a_{l,m}\delta_{l,l-1}\delta_{m,m-1}\int_0^{r_{max}} u_{kl}\left(\frac{du_{k^{'},l-1}}{dr} - \frac{l}{r}u_{k^{'},l-1}\right)dr \\
&-a_{l+1,m+1}\delta_{l,l+1}\delta_{m,m+1}\int_0^{r_{max}} u_{kl}\left(\frac{du_{k^{'},l+1}}{dr} + \frac{l+1}{r}u_{k^{'},l+1}\right)dr \\
&-a_{l+1,-m+1}\delta_{l,l+1}\delta_{m,m-1}\int_0^{r_{max}} u_{kl}\left(\frac{du_{k^{'},l+1}}{dr} + \frac{l+1}{r}u_{k^{'},l+1}\right)dr
\end{aligned} \tag{2.64}$$

Where the a_{lm} constant is defined as in equation (2.65).

$$a_{lm} = \sqrt{\frac{(l+m)(l+m-1)}{4(2l-1)(2l+1)}} \tag{2.65}$$

Each of the four integrals in equation (2.64) has two Kronecker delta functions associated with it, one for each of m and l. These Kronecker delta functions give rise to the selection rules, since they will only be non-zero when $l = l^{'}\pm 1$ and $m = m^{'}\pm 1$. The p_x element can be derived in a similar manner, and is shown in equation (2.66). The selection rules and magnitudes of each integral are identical to the p_y elements, but each integral now has a complex component, and sign alternation for the first and last integrals.

$$
\begin{aligned}
-i\langle\frac{u_{kl}(r)}{r}Y_l^m(\theta,\varphi)|\frac{\partial}{\partial x}|\frac{u_{k'l'}(r)}{r}Y_{l'}^{m'}(\theta,\varphi)\rangle = \\
+ia_{l,-m}\delta_{l,l-1}\delta_{m,m+1}\int_0^{r_{max}} u_{kl}\left(\frac{du_{k',l-1}}{dr}-\frac{l}{r}u_{k',l-1}\right)dr \\
-ia_{l,m}\delta_{l,l-1}\delta_{m,m-1}\int_0^{r_{max}} u_{kl}\left(\frac{du_{k',l-1}}{dr}-\frac{l}{r}u_{k',l-1}\right)dr \\
-ia_{l+1,m+1}\delta_{l,l+1}\delta_{m,m+1}\int_0^{r_{max}} u_{kl}\left(\frac{du_{k',l+1}}{dr}+\frac{l+1}{r}u_{k',l+1}\right)dr \\
+ia_{l+1,-m+1}\delta_{l,l+1}\delta_{m,m-1}\int_0^{r_{max}} u_{kl}\left(\frac{du_{k',l+1}}{dr}+\frac{l+1}{r}u_{k',l+1}\right)dr
\end{aligned}
\tag{2.66}
$$

The p_z element is given in equation (2.67), where the selection rule for m can be seen to be $\Delta m = 0$,

$$
\begin{aligned}
-i\langle\frac{u_{kl}(r)}{r}Y_l^m(\theta,\varphi)|\frac{\partial}{\partial z}|\frac{u_{k'l'}(r)}{r}Y_{l'}^{m'}(\theta,\varphi)\rangle = \\
-ib_{l,m}\delta_{l',l-1}\delta_{m',m}\int_0^{r_{max}} u_{kl}\left(\frac{du_{k',l-1}}{dr}-\frac{l}{r}u_{k',l-1}\right)dr \\
-ib_{l+1,m}\delta_{l,l+1}\delta_{m',m}\int_0^{r_{max}} u_{kl}\left(\frac{du_{k',l+1}}{dr}-\frac{l}{r}u_{k',l+1}\right)dr
\end{aligned}
\tag{2.67}
$$

and where the b_{lm} constant is defined as in equation (2.68).

$$
b_{lm} = \sqrt{\frac{l^2-m^2}{(2l-1)(2l+1)}} \tag{2.68}
$$

2.5 Time Propagation

The final step is to propagate the system through time. This time propagation works by solving the *time dependent* Schrödinger equation (TDSE), shown in (2.69).

$$
i\hbar\frac{\partial}{\partial t}\Psi(r,\theta,\varphi,t) = H\Psi(r,\theta,\varphi,t) \tag{2.69}
$$

In order to express the TDSE on matrix form, we expand the total wave function as a linear combination of the previously found bound and scattered states, as shown in equation (2.70).

$$
\Psi(r,\theta,\varphi,t) = \sum_{l=0}^{l_{max}}\sum_{m=-l}^{l}\sum_{k=1}^{N} c_{klm}(t)\psi_{klm}(r,\theta,\varphi) \tag{2.70}
$$

It can be shown that by substituting this wave function into the TDSE, one can derive the new matrix representation in equation (2.71).

$$
i\hbar\frac{\partial}{\partial t}\begin{pmatrix} c_1(t) \\ . \\ . \\ c_i(t) \\ . \\ c_n(t) \end{pmatrix} = \begin{pmatrix} H_{1,1} & H_{1,2}(t) & . & . & . & H_{1,n}(t) \\ . & . & & & & . \\ . & . & . & & & . \\ H_{i,1}(t) & H_{i,2}(t) & . & H_{i,i} & . & H_{i,n}(t) \\ . & . & & & . & . \\ H_{n,1}(t) & H_{n,2}(t) & . & H_{n,i}(t) & . & H_{n,n} \end{pmatrix} \begin{pmatrix} c_1(t) \\ . \\ . \\ c_i(t) \\ . \\ c_n(t) \end{pmatrix} \tag{2.71}
$$

The time dependent coefficients $c_i(t)$ are related to the corresponding wave function ψ_{klm} by equation (2.72).

$$i = N * (l(l+1) + m) + k \tag{2.72}$$

The coefficients are then found by solving the equations of the Hamiltonian, using a technique developed by Shampine and Gordon [28].

2.5.1 Initial and End States

The simulation has to be initialized in a certain state at time (t = 0). In this thesis, I work with the pure 5g(m=4) Rydberg state, meaning coefficients for all other states were set to zero. After the simulation has been performed at time (t=T), most likely we have transitioned from the pure initial state, to a distribution among all the different possible states. An example of this transitioning is illustrated in (2.73).

$$(t=0) \rightarrow \begin{pmatrix} 0 \\ . \\ . \\ c_{5g(m=4)} = 1 \\ . \\ . \\ 0 \end{pmatrix} \rightarrow \begin{pmatrix} 0.0001 \\ . \\ 0.0156 \\ 0.6534 \\ 0.2140 \\ . \\ 0.0001 \end{pmatrix} (t=T) \tag{2.73}$$

I have now covered the theoretical groundwork necessary to produce the results obtained as part of this thesis, which I will present in the next chapter.

Chapter 3

Results

In this chapter I will present the results for all the different simulations that have been performed as part of this thesis. The first part consists of testing the developed procedure by reproducing some ionization probability curves from a previously published article [1]. After, I will discuss the effect that different orientations of the circular polarized fields have on the ionization probability and on other quantities, such as the angular distribution. The first orientations under investigation are the co- and counter-rotating fields, as illustrated in figure (3.1a) and (3.1b), respectively.

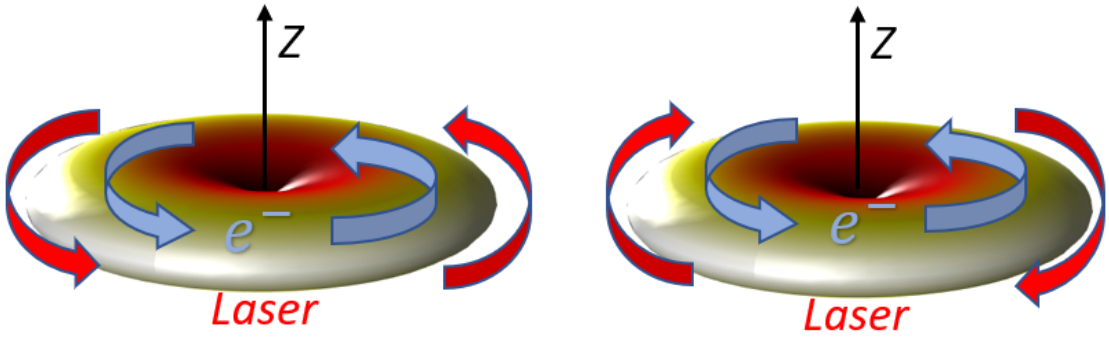

(a) Co-rotation (b) Counter-rotation

Figure 3.1: The figure illustrates the co- (a) and counter-rotating fields (b), in relation to the rotational motion and geometry of the electron distribution of the 5g(m=4) state.

3.1 Co- and Counter-Rotating Polarized Fields

In the previous section, it was mentioned that there had already been done theoretical simulations using circularly polarized laser pulses on the circular 5g(m=4) state [1]. In the referred article they documented a stabilization effect of the ionization

probabilities, observed when increasing the laser intensity beyond a certain point. This effect is counter intuitive, since the natural assumption is that the ionization probability should increase when increasing the laser intensity. Since I will investigate the same system, it was natural to try and reproduce the ionization probability curves. The article documented ionization probabilities for several different laser cycles, so for the comparative simulation, I chose a four-cycle ($N_c = 4$) laser pulse, using the same 800 nm wavelength laser, having frequency $\omega = 0.057$ (a.u.). For all my simulations I used the smallest box mentioned in the article of 600 (a.u.) and an upper limit of $l_{max} = 15$. Also, E_{max} was set to 7.5 (a.u.) leading to N = 740 basis functions for each eigenstate problem. The rotation of the electric field was induced by introducing a relative phase difference of $\varphi = \pi/2$ between the x and y component of the laser, as has been previously discussed in section (2.3.4).

The reproduced ionization probabilities for the co-rotating field can be seen in figure (3.2a) and the result for the counter-rotating field in figure (3.2b). The reference data from [1] is plotted with a red-dashed line, while the blue line is the reproduced results. The reproduction of ionization probabilities for the counter-rotating case (figure (3.2b)), were almost identical to the results obtained in the referred article, for field intensities below $E_0 = 0.06498$ (a.u.), with an observed deviation for intensities above this region (separation of blue and red curves). Even though the curves separate, it is evident that the stabilization effect is present in the reproduced result, where the ionization probability decreases after having reached a maximum at a lower intensity.

The co-rotating case in figure (3.2a) proved to be a slightly more difficult case to reproduce. Nevertheless, there seem to be a good agreement between my result and the result of the article, for field intensities below $E_0 = 0.06$ (a.u.). The simulation performed in the reference article can be considered to be more trustworthy than my thesis simulation, since it was done with larger box limits in the range between 600 and 2000 (a.u.). They also used a much larger upper bound for l_{max}, having $l_{max} = 41$ for intensities where $E_0 \leq 0.3$ (a.u.), and $l_{max} = 63$ otherwise. Nevertheless, there is a slight deviation in the ionization probability just below $E_0 = 0.03$ (a.u.) and $E_0 = 0.02$ (a.u.), which is well within the trusted intensity region and where I expected the results to be identical. The deviation in my data has captured what seems to be a small stabilization effect for $E_0 \approx 0.03$ (a.u.), not present in results of the original publication. One possible explanation is that the reference curve has been constructed by interpolation, and which did not include a sufficient number of points to capture the full ionization structure.

In the article, they also argue that the steeper ionization curve in (3.2a), can be explained by the electric field rotation being in the same direction as the motion of the electron. From here, they make an analogy about a classical *sling-shot effect*, caused by the electron experiencing a greater time of acceleration and deceleration in the co-rotating case, than in the counter-rotating case.

The difference between the co- and counter-rotating fields can also be observed by looking at the differential probability vs. kinetic energy for the electron at a given field intensity. This was done, and the kinetic energy distribution for the electron in the co-rotating field can be seen in figure (3.3a), and for the counter-rotating field in figure (3.3b). Clearly, the probability for finding the electron at larger kinetic energies is significantly lower for the counter-rotating field, than the co-rotating field at the same field intensity of $E_0 = 0.02$ (a.u.). This result is somewhat expected,

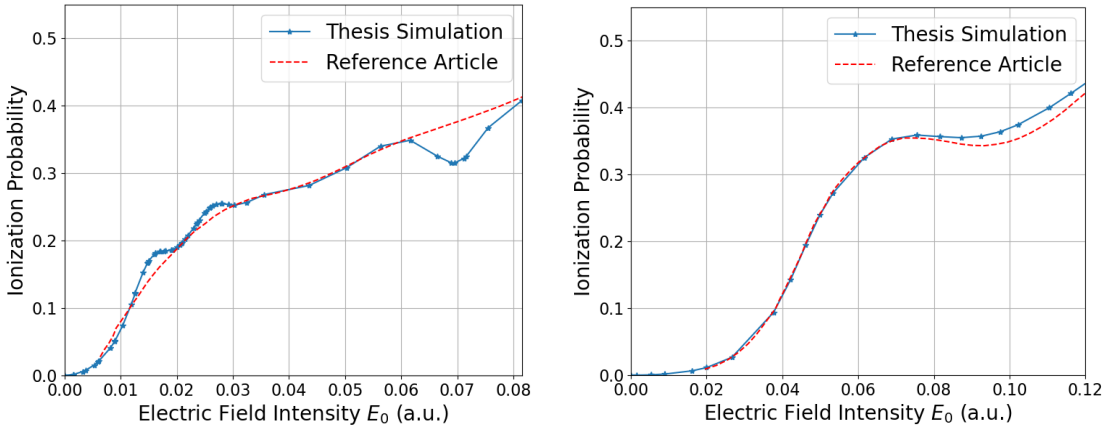

(a) Co-rotating field (b) Counter-rotating field

Figure 3.2: **a)** Ionization probability using a co-rotating field at different field intensities, having the circular 5g(m=4) as initial state. The blue curve are the reproduced results from simulations performed as part of this thesis. The data from the red curve has been obtained from a reference article that had done identical simulations, but having used a larger basis [1]. **b)** The same simulation as in (a), but from a counter-rotating field.

from the fact that the co-rotating field displayed a steeper ionization probability curve.

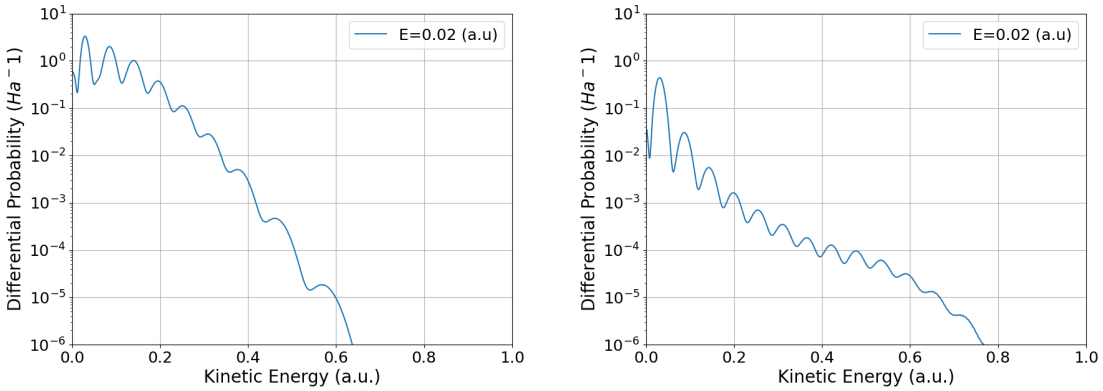

(a) Co-rotating field (b) Counter-rotating field.

Figure 3.3: **a)** Differential probability vs. kinetic energy for the co-rotating field. **b)** Differential probability vs. kinetic energy for the counter-rotating field. Both curves results from a simulation performed at a field intensity of $E_0 = 0.02$ (a.u.).

Also, to further increase the confidence that the simulation output was not highly effected by restricting the box size (r_{max}) to 600 (a.u.), and the higher-energy quantum states (l_{max}) to 15, several convergence tests were performed. The tests were performed by selecting a reasonable high intensity of $I_0 = 1 \times 10^{14}$ W/cm^2, corre-

sponding to $E_0 = 0.05338$ (a.u.), and then fixating one of either r_{max} or l_{max} at a specific value, while increasing the other until convergence. The result for the l_{max}-convergence test can be seen in figure (3.4a), where the upper bound for the box size was set to $r_{max} = 400$ (a.u.). From the figure, it can be seen that there is a large improvement in the ionization probability when going from l_{max} 5 to 10, and l_{max} 10 to 15, but a very small change when going from l_{max} 15 to 20, and so it suggests that an l_{max} of 15 is sufficient for achieving reasonable results at this intensity level. The convergence-test for the box size (r_{max}) was performed by fixating l_{max} at 15 for all simulations, and the results can be seen in figure (3.4b). Here the change in ionization probability is on a much smaller scale for the selected r_{max} values, than it was in the l_{max} case. Nevertheless, the important point is that there is a very small change in the ionization probability, when increasing the box size from 400 (a.u.) to 600 (a.u.), indicating that a further increase of the box size, would have very little effect on the overall ionization probability. The results from both convergence tests suggest that an upper limit for l_{max} at 15, and a box size of 600 (a.u.), is more than enough for calculating ionization probabilities at a reasonable accuracy, at an intensity region below or slightly above $E_0 = 0.05338$ (a.u.).

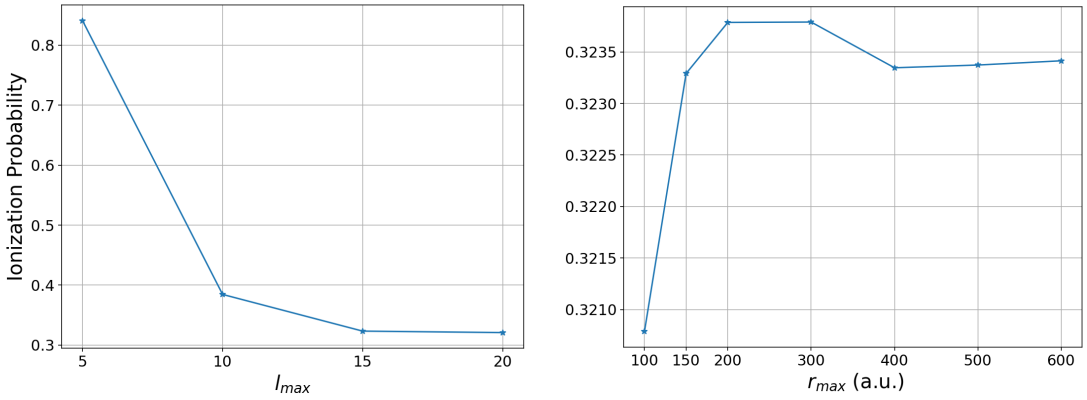

(a) Ionization probability vs. l_{max}.

(b) Ionization probability vs. r_{max}.

Figure 3.4: In the figure, the results from l_{max} and r_{max} convergence tests are shown, both having been performed at the same intensity of $E_0 = 0.05338$ (a.u.), under the same co-rotating field as in figure (3.2a). **a)** Plot of ionization probability vs. l_{max}. All simulations were performed by fixating r_{max} at 400 (a.u.), and convergence was reached at $l_{max} = 15$. **b)** Plot of ionization probability vs. r_{max}, having l_{max} fixed at 15 for all simulations. Convergence was reached at $r_{max} = 600$ (a.u.).

Regardless, treating the values from the reference data as some sort of trusted benchmark with respect to the ionization curves, in further simulations, I therefore consider the field intensity $E_0 = 0.06498$ (a.u.) as an upper bound for intensities that should be considered accurate. This threshold is equivalent of $I_0 = 1.48 \times 10^{14}$ W/cm^2, which is slightly above the convergence test intensity. However, even if the simulation output might be considered somewhat inaccurate for intensities above this threshold, I still believe it is highly likely that the general form of the curves, will have a similar shape as more computationally exhaustive simulations. For example that my thesis simulation deviates from the reference curve in figure (3.2b), but

nevertheless has captured the overall reduction in ionization probability, up to a field intensity of $E_0 = 0.06498$ (a.u.). Therefore, when including intensities beyond this region, it will be emphasized by plotting a dotted line.

The next section covers a discussion of the electron angular distributions for the co- and counter-rotating fields.

3.2 Angular Distributions: Circular Fields

The electron angular distributions for the ionized states contain information on the likelihood for the electron to be ejected along a specific path, determined by the angles θ and φ. If every path is equally likely, then the resulting distribution would be a completely symmetrical sphere. It would be of interest to know what the resulting form of these distributions look like for the different types of polarized fields, but also for different laser intensities. I first looked at the distributions belonging to the co-rotating field.

3.2.1 Angular Distributions: Co-Rotating Field

For the co-rotating field, I first calculated angular distributions at two different intensity values. The results are displayed in figure (3.5), where the distribution from the smallest intensity (1) $E_0 = 0.00162$ (a.u.) is placed on top of the distribution from the larger intensity (2) $E_0 = 0.00505$ (a.u.). Both distributions have the same overall shape as the initial state 5g(m=4). The span in the x and y directions of the smallest distribution (1), is 1/10th the span of the respective x and y components of the larger distribution (2), I therefore scaled the x and y axis of the smallest distribution by a factor of 5, to enlarge it to its current size. There are two main takeaways from the figure; the first is that increasing the intensity increases the size of the distribution, which reflects the increased total ionization yield from $P_{ion} = 0.001$ to $P_{ion} = 0.015$. The second is that the ejection paths of the electron remain unchanged at these intensity levels, which might be from the fact that we are effectively dealing with single photon absorption in both cases.

In order to understand how the angular distribution evolves over a larger intensity range, several additional distributions were calculated at larger intensities. Thereafter, the angular distributions were combined with the corresponding ionization probabilities into a single figure. The results are shown in figure (3.6), where one can observe the evolution from a circular torus shape at low intensities, to more pancake-shaped distributions having out-off plane ejection orbits around the torus cavity, at larger intensities. The common feature over the whole intensity range is that the electrons are mostly ejected within the xy-plane, which I will try to explain after discussing the results from the counter-rotating field in the next section.

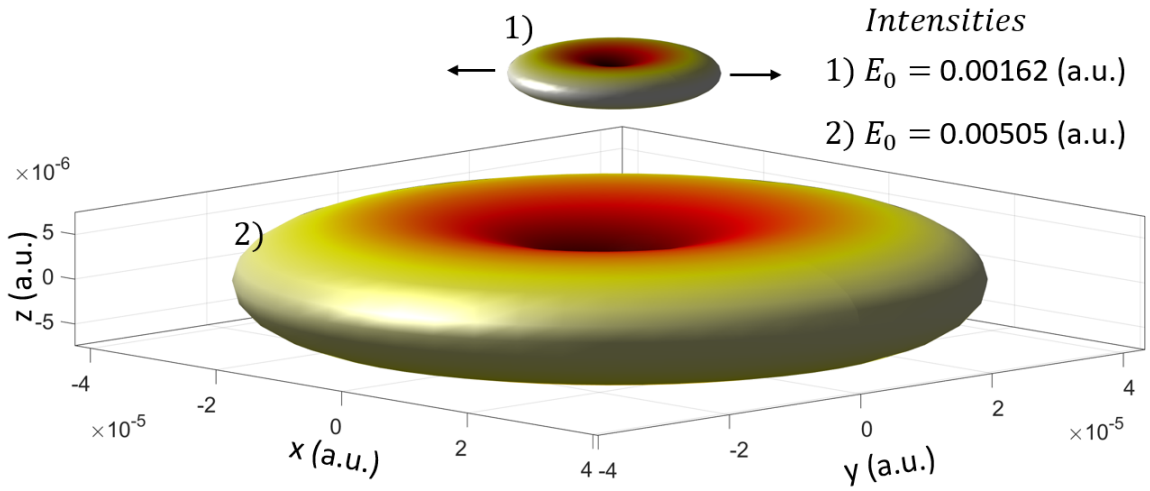

Figure 3.5: Angular distributions from simulations having a co-rotating field. The smallest torus **1)** on top was calculated for an intensity of $E_0 = 0.00162$ (a.u.), while the larger at the bottom **2)** with $E_0 = 0.00505$ (a.u.). The figure demonstrates that both angular distributions have a similar shape as the initial 5g(m=4) state, but experience a scaling by a factor of 10 in the x, y dimensions, when going from intensity (1) to intensity (2).

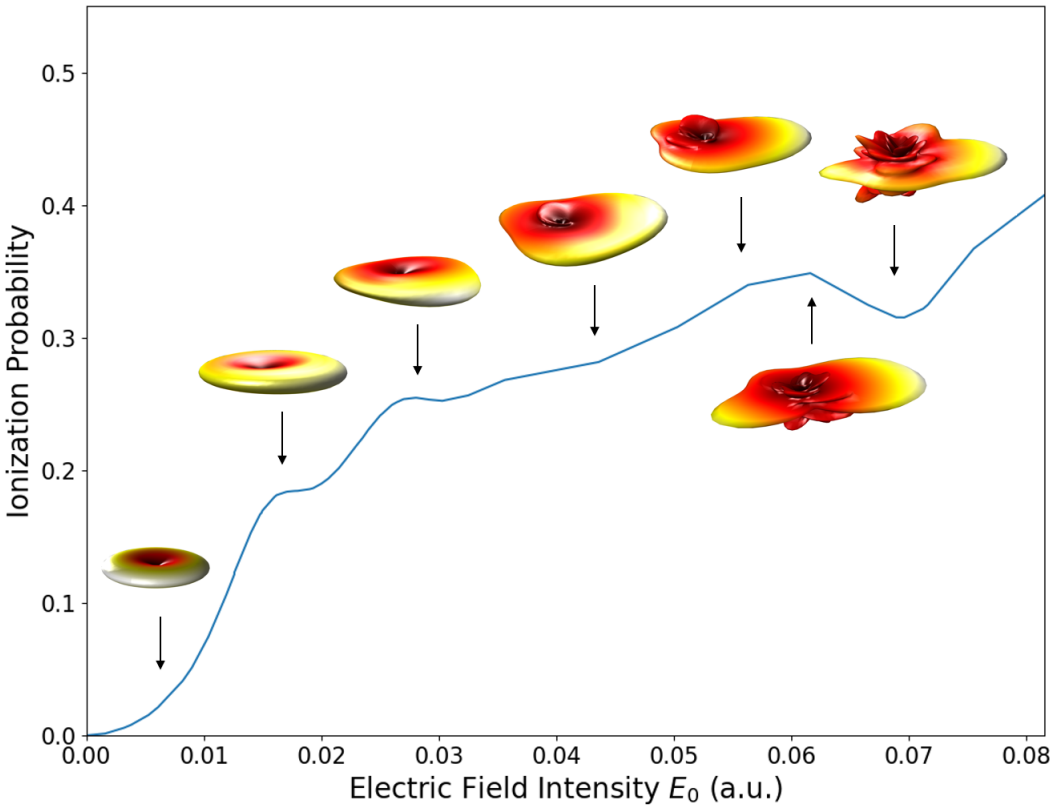

Figure 3.6: The evolution of angular distributions for the co-rotating field. The evolution shows that a circular geometry dominates throughout the intensity sweep for the co-rotating field, but that new out-off plane ionization trajectories forms around the torus cavity at large intensities. Also note that the distributions are not to scale.

3.2.2 Angular Distributions: Counter-Rotating Field

The investigation of the angular distributions originating from the counter-rotating field were performed at almost identical intensity values, as the co-rotating comparison. The results are are displayed in the two-panel figure (3.7a) and (3.7b).

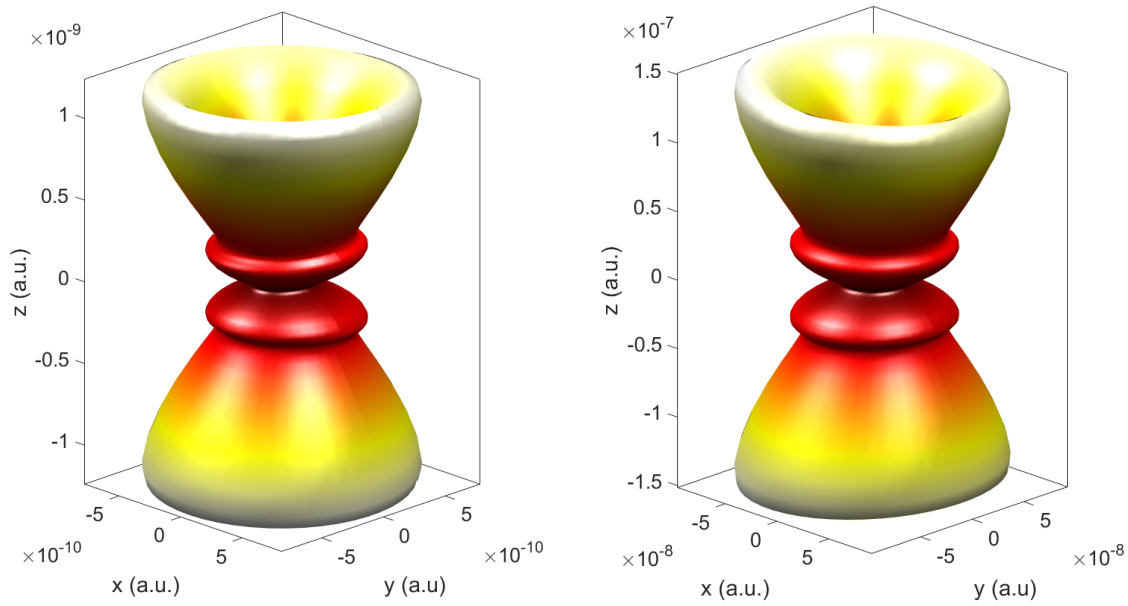

(a) Counter rotation: $E_0 = 0.00162$ (a.u.). (b) Counter rotation: $E_0 = 0.00527$ (a.u.).

Figure 3.7: Comparison between two angular distributions from simulations having a counter-rotating electric field. Figure (a) displays the result from the smallest intensity of $E_0 = 0.00162$ (a.u.), while figure (b) shows the larger intensity of $E_0 = 0.00527$ (a.u.). The figure demonstrates that the circular geometry of the torus is broken, when the electric field rotates in the opposite direction of the electron motion, and that the distribution-span in the xy-dimensions, are three orders of magnitude smaller than for the equivalent spans in the co-rotating cases.

It can be seen from the figure that the circular geometry of the torus has been broken, leaving us with cone-shaped angular distributions. One of the key differences in the results between the cone and the torus from the co-rotating field, is that the span of the distribution along the x and y axis are found to be three orders of magnitudes smaller, reflecting the lower ionization probability. Also, the most extreme difference between the torus- and cone-shape is located in the xy-plane at z = 0, which transformed from the most probable, to the least probable region to be ejected from in the counter-rotating field.

The evolution of angular distributions over a larger intensity range was also created for the counter-rotating cases, by plotting selected distributions on top of the corresponding ionization probability curve, which can be seen in figure (3.8). From the evolution figure it can be seen that we start of with the cone-shaped distribution at low intensities, followed by pillar-shaped distributions at intermediate intensities, and lastly a combination between a disk and a pillar for large intensities. The evolution of the counter-rotating shapes are vastly different than what we observed for the co-rotating field in figure (3.6). Now, the dominant spatial direction is in the z-direction, opposite of what was observed for the evolution to the co-rotating field.

However, at larger intensities there seem to be a similarity between the counter- and co-rotating cases, from the fact that both display distributions that have formations of ejection trajectories close to the center of the original torus cavity. This might be an anomaly or maybe a few-cycle effect, considering we are using a 4-cycle laser pulse. The 4-cycle pulse has a total duration of 440 (a.u.), which leads to a time of 110 (a.u.) per revolution. The time for each revolution is then found to be close to 1/8th of the electron's classical orbital period of 785 (a.u.). The orbital period for the electron in the 5g(m=4) state was found considering a classical model, and the full calculation can be read in appendix (C.1).

Since the rotational frequency of the laser is on the same order of magnitude as the orbital period of the electron, we expect the rotational direction to play a role, as we saw from the difference in ionization curves and angular distributions. One way to think about this, will be to consider the electron distribution at two different sides of the torus. If the laser is initialized to be parallel to the electron velocity at one side, then it will be anti-parallel at the other side. If we now have that the orbital period of the electron is the same as that of the laser, then the distribution starting with a parallel field will continue to have so throughout the revolution, considering no change in velocity for the electron.

However, for larger circular Rydberg states the orbital period increases significantly, and so one would expect the rotation to play a smaller role in these cases, due to the rotation of the field being so much faster than that of the electron. This has been documented for the circular $10l(m = 9)$ state, which show much more similar ionization curves for the co- and counter-rotating cases [1].

In order to explain the dominant circular shape of the distributions belonging to the co-rotating field in figure (3.5), one must consider the electron orbits in the states that are most probable for transition. The reason is that the electron will experience a push from the laser when orbiting, and so the overall angular distribution represent average ejection paths over all possible orbits of that occupied state, and should therefore have a similar shape to the corresponding spherical harmonic. For single photon absorption the selection rules for the co- and counter-rotating fields have been found to be as in equation (3.1) [1].

Co-rotation	**Counter-rotation**	
$\Delta m = +1$	$\Delta m = -1$	(3.1)
$\Delta l = +1$	$\Delta l = \pm 1$	

Now, in all simulations we have the circular 5g(m=4) or 4l(m=4) as initial state, and if we start by looking at the co-rotating field, then from the co-rotating selection rule in (3.1), we have 5l(m=5) as the next excited state. This can also be recognized to be a circular state, which means that all ejection paths will originate from circular orbits, and can explain why the angular distributions keeps the circular shape when we are dealing with low intensity or single-photon absorption. For larger intensities the dominant shape still seem to be circular, but the overall distribution is probably a combination between states having non-circular orbits due to the transition rule not being totally absolute in the high-intensity regime.

For the counter rotating case the selection rules leads to two possible transitions; one state having l=3, m=3, and the other having l=5, m=3. It was believed that the overall cone-shape could be explained to be a combination between these two states. This was tested by taking an equally weighted linear combination of the spherical

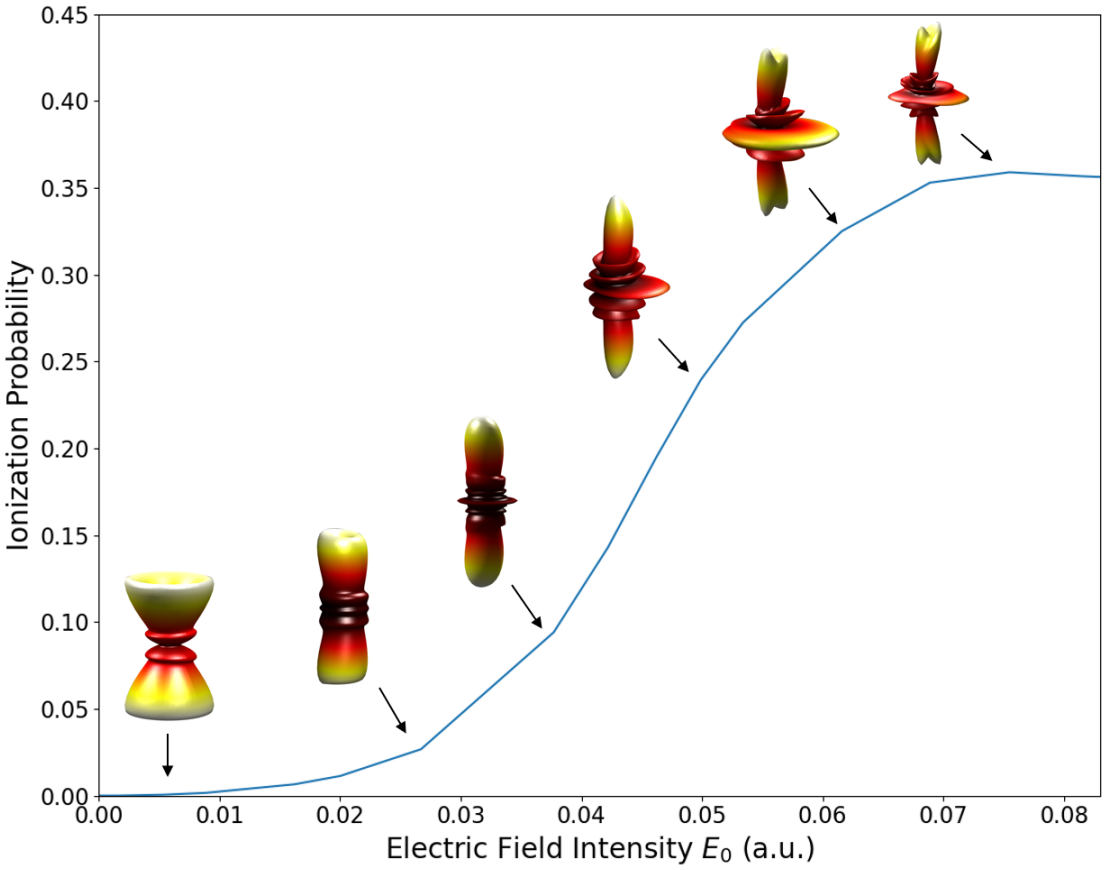

Figure 3.8: The evolution of angular distributions, resulting from a field that counter-rotates the motion of the electron, shown side by side with the corresponding ionization probability. The evolution shows that a pillar-shape dominates at low intensities, but that a growing circular disk forms at larger intensities. Also note that the distributions are not to scale.

harmonics $Y_l^m(\theta, \varphi)$ as such; $Y_3^3(\theta, \varphi)+Y_5^3(\theta, \varphi)$, and then plotting the absolute value of the combined spherical harmonic as the radius in a spherical coordinate system. The plot of each individual harmonic can be seen in figure (3.9a) and (3.9b), while the plot from the linear combination can be seen in figure (3.9c). It can be seen that the geometry of the linear combination closely resemble the cone-shaped angular distribution at low intensities for the counter-rotating field.

Also, if we assume the selection rule somewhat holds for multi-photon absorption, then in all transitions we have that the m-value must decrease (Δm= -1). This means we must pass the m = 0 state after a certain number of transitions. The m = 0 state has a lobe in the z-direction for most l-values, where an example can be seen for the 5g orbitals in figure (1.1). Therefore, if we pass the general state l^*(m=0), we expect there to be some z-directionality to the angular distribution. This hypothesis can explain some of the angular distributions observed at larger intensities for the counter-rotating field, seen in figure (3.8). Another key observation is that if we start off at the positive side of m-values (as we do in 5g(m=4)), then after a number of transitions we will find ourselves in the negative m-regime. Effectively, this is equivalent to a reversal of the electronic rotational direction, that occurs when the field counter rotates the electron motion.

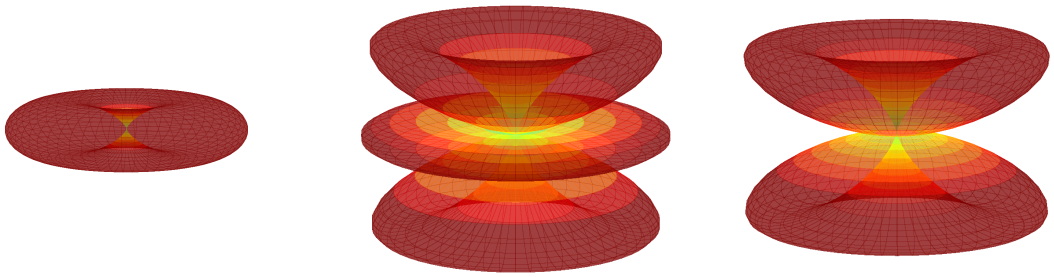

(a) $|Y_l^m(\theta,\varphi)|$ l=3, m=3 (b) $|Y_l^m(\theta,\varphi)|$ l=5, m=3 (c) $|Y_3^3(\theta,\varphi) + Y_5^3(\theta,\varphi)|$

Figure 3.9: The figure illustrates that the cone geometry of the angular distribution from the counter-rotating field, can be explained to result from the linear combination of spherical harmonics between the two possible transition states for single-photon absorption. Each figure is created by using the absolute value of these spherical harmonics as the radius in a spherical coordinate system. (a) shows the result from spherical harmonic $Y_l^m(\theta,\varphi)$ having l=3, m=3. (b) for $Y_l^m(\theta,\varphi)$ having l = 5, m = 3. c) shows the linear combination of the spherical harmonics in (a) and (b). Each plot was created in Python using the *sph-harm* package from the SciPy libray to calculate spherical harmonics.

I am now done discussing the co- and counter-rotating fields. In the next section, I will investigate the results from the perpendicular-rotating xz-polarized field. An illustration of how the geometry of the laser relates to the geometry of the 5g(m=4) state, can be seen in figure (3.10).

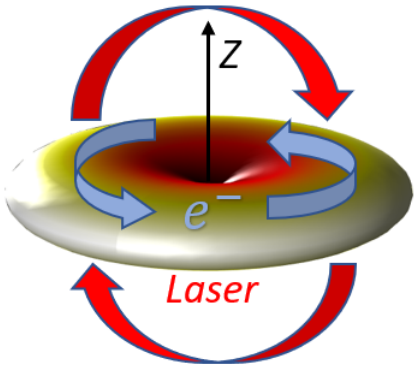

Figure 3.10: Illustration of the xz-polarized rotating field, in relation to the electron distribution of the 5g(m=4) state.

3.3 Perpendicular Rotating Fields

The xz-polarized field that rotated perpendicular to the electron distribution of the 5g(m=4) state, was implemented by including the $A_x(t)$, $A_z(t)$ components of the laser, and setting the relative phase difference between them to $\varphi_x = 0$, $\varphi_z = \pi/2$. A total of 45 simulations were conducted, having a linear intensity spacing in the

interval $E_0 \in [0, 0.09747]$ (a.u.). The matrix elements were constructed using the same basis of $r_{max} = 600$ (a.u.), $l_{max} = 15$, $E_{max} = 7.5$ (a.u.), $N = 740$, $Nb = 890$, and identical parameters for the laser $\omega = 0.057$ (a.u.), $N_c = 4$. The resulting ionization probability curve for the perpendicular field orientation can be see in figure (3.11), where the dotted blue line represent data points beyond the trusted threshold of 0.06498 (a.u.). The red line correspond to additional simulation points where the l_{max} value has been increased to 20, which gave close to identical results within the trusted region, but started to deviate slightly when entering the beyond trusted region, which is in accordance with expectations.

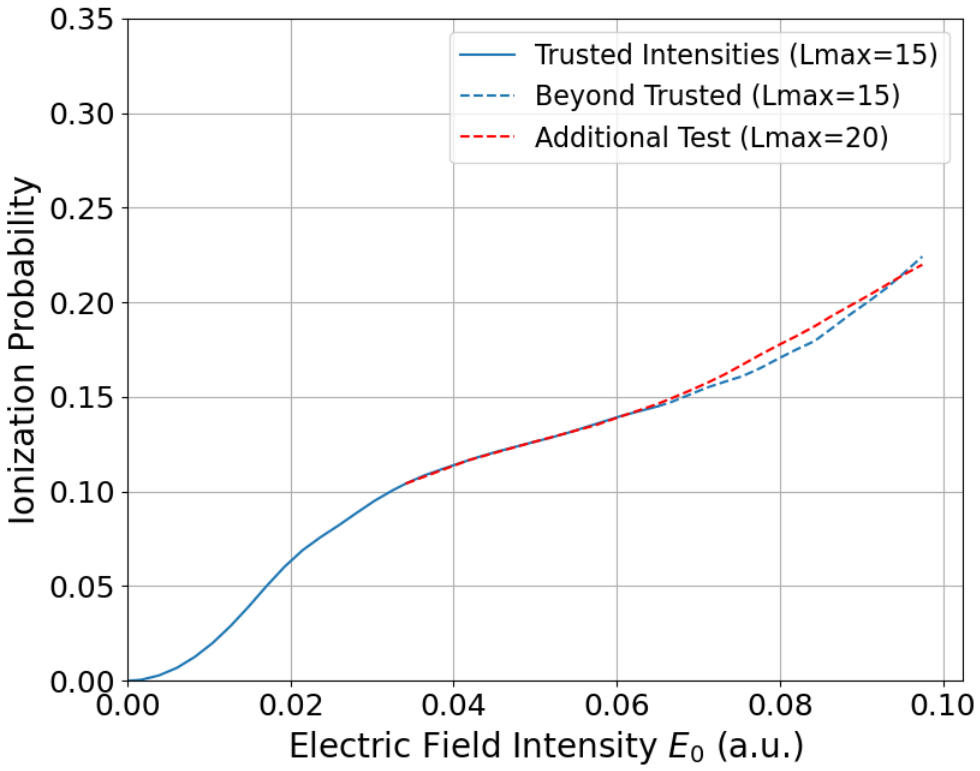

Figure 3.11: Ionization probability curve for the xz-polarized field, rotating perpendicular to the torus-shaped electron distribution of the 5g(m=4) state. The curve was created from ionization probabilities produced from 45 individual simulations, having a linear separation of intensities in the interval $E_0 \in [0, 0.09747]$ (a.u.).

Comparing the ionization probability curve from the xz-polarized field, with the corresponding curves for the in-plane co- and counter-rotating fields in figure (3.2b) and (3.2a), it can be seen that the ionization probability is lower at identical intensities, when the field rotates perpendicular to the plane of the electron distribution. For example at the threshold region at $E_0 = 0.06498$ (a.u.), the perpendicular xz-rotating field produced an ionization probability of $P_{ion} = 0.15$, which is less than half of the corresponding $P_{ion} = 0.35$ ionization probability for the counter-rotating field, observed in figure (3.2b). The observation that the in-plane rotating fields returns a steeper ionization probability curve than the perpendicular rotating field, might be explained by an analogy with simple classical motion. It is naturally to think that if the field have all components in the same plane as the electron rotates within, then the maximum possible change of velocity will occur when all the vector components align. There is only one component to align between the motion of

the electron in the xy-plane, and the perpendicular xz-polarized field, and so it is no surprise that the ionization probability is lower. Nevertheless, the shape of the curve is rather similar to the in-plane fields, where the ionization probability display a similar increase in value, also having the characteristic change from a convex to concave shape at $E_0 \approx 0.03$ (a.u.). Lastly, as can be observed from the "beyond trusted" region, there is no sign of the stabilization effect that was present for the in-plane co- and counter-rotating fields.

It is also of interest to investigate the distribution of kinetic energies for the electron at different field intensities. This was done by plotting three selected differential probability curves against the kinetic energy of the electron, which can be seen in figure (3.12). The probability for finding the electron at a given energy interval, is given by the area under the curve for that interval. The oscillating spikes in probabilities occur at an even energy spacing, and can be reasoned to result from *multi-photon resonances*, where the distance between each peak should equal a single photon energy. The first peak correspond to a net-absorption of a single photon, the second of two and so on. However, it must be emphasized that the electron can also re-emit photons, and so in reality there might be a larger net number of photons involved than the specific numbering of the resonance peak. The elevation of the probability curves in figure (3.12) illustrates that the probability for measuring the electron at a larger kinetic energy increases rapidly with intensity. This is an expected result, since intensity is in reality related to the average number of photons (N_p) present in the laser pulse, having total energy of ($E = N_p * hf$). Therefore, larger intensities increases the probability for multi-photon absorption.

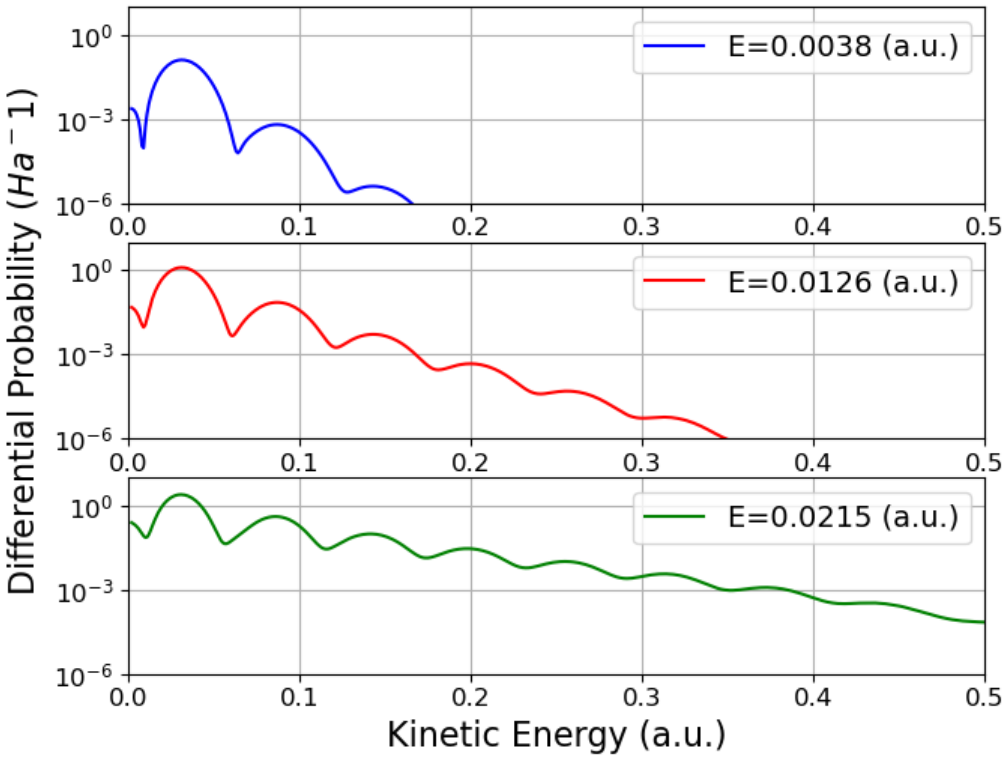

Figure 3.12: Three selected differential probability vs. kinetic energy plots for the circular xz-polarized field. The intensities are 0.0038 (a.u.), 0.0126 (a.u.) and 0.0218 (a.u.), from top panel to bottom panel respectively.

3.3.1 Angular Distributions: Perpendicular Field

The first investigation of the angular distributions related to the perpendicular xz-polarized field were performed at an intensity of $E_0 = 0.00162$ (a.u.), which correspond to the absorption of a single-photon. A four-panel figure where this distribution has been viewed from four different angles, can be seen in figure (3.13a)-(3.13d).

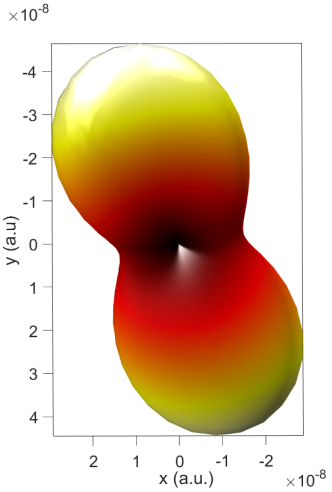

(a) View (a).

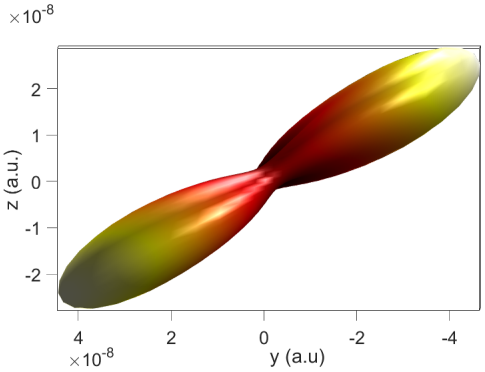

(b) View (b).

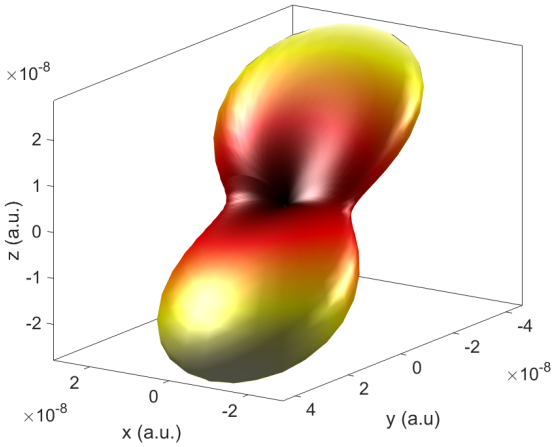

(c) View (c).

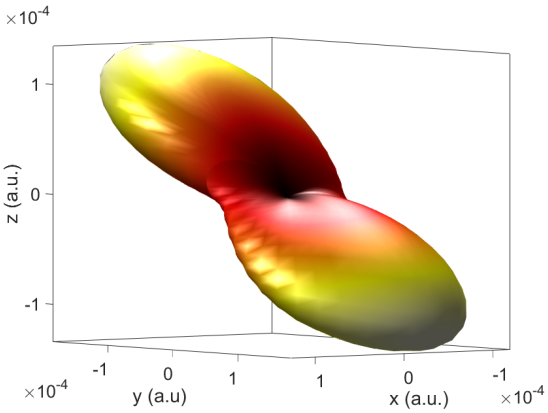

(d) View (d).

Figure 3.13: Four-panel figure displaying different planes of view on the same angular distribution from the xz-polarized field, resulting from an intensity of $E_0 = 0.00162$ (a.u.).

The occupation of scattered states belonging to the distribution in figure (3.13a)-(3.13d), were investigated and it was found that the most populated states consisted of three different m, l combinations; one having l=5, m=5, another having l=5, m=4 and the last having l=3, m=3. The l=5, m=4 combination can be recognized to come from the selection rule related to the z-polarization ($\Delta l = +1$, $\Delta m = 0$), while

the two other l, m pairs come from the x-related selection rules. A linear combination was calculated between the three spherical harmonics, where each spherical harmonic was weighted with the corresponding complex coefficient. The absolute value of the linear combination was plotted as the radius in a spherical coordinate system, and the resulting geometry can be seen in figure (3.14a) and (3.14b). The directional orientation of this geometry is not completely identical to that of the calculated angular distribution, which is probably because there is a significant contribution from states other than the three most populated ones.

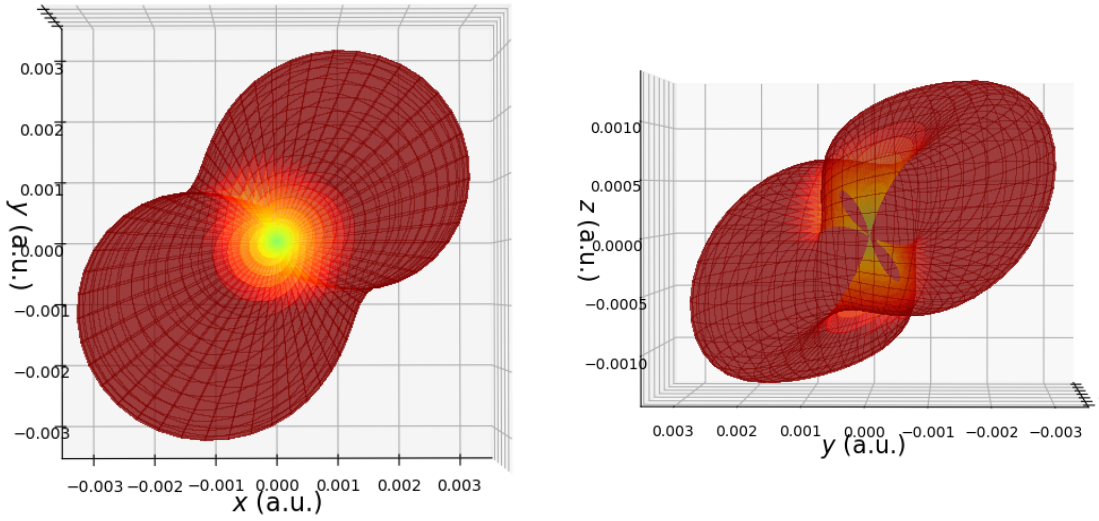

(a) View (1). (b) View (2).

Figure 3.14: Resulting shape for plotting the absolute value of the linear combination between the three individual harmonics $Y_l^m(\theta, \varphi)$ having l=5, m=5, l=5, m=4 and l=3, m=3, as $|a_1 Y_5^4(\theta, \varphi) + a_2 Y_5^5(\theta, \varphi) + a_3 Y_3^3(\theta, \varphi)|$. These three m, l combinations belong to the most occupied scattered states from the xz-polarized field, where a_1, a_2, a_3 are the corresponding complex coefficients for each of the three states.

The evolution of angular distributions were also investigated by combining them with the corresponding ionization probabilities, as were done when investigating the previous field orientations. Figure (3.15) shows the overall evolution from what looks like a 2-blade propeller at low intensities, to more chaotic structures at larger intensities. It is very plausible that the last four distributions are not completely converged given their "spiky" shapes, but which does not necessarily mean that the ionization yields are not correct. The calculation of ionization yields is less sensitive to slight deviations in simulation-output than the calculation of angular distributions.

Lastly, I will present a summary and conclusion of the study carried out in this thesis.

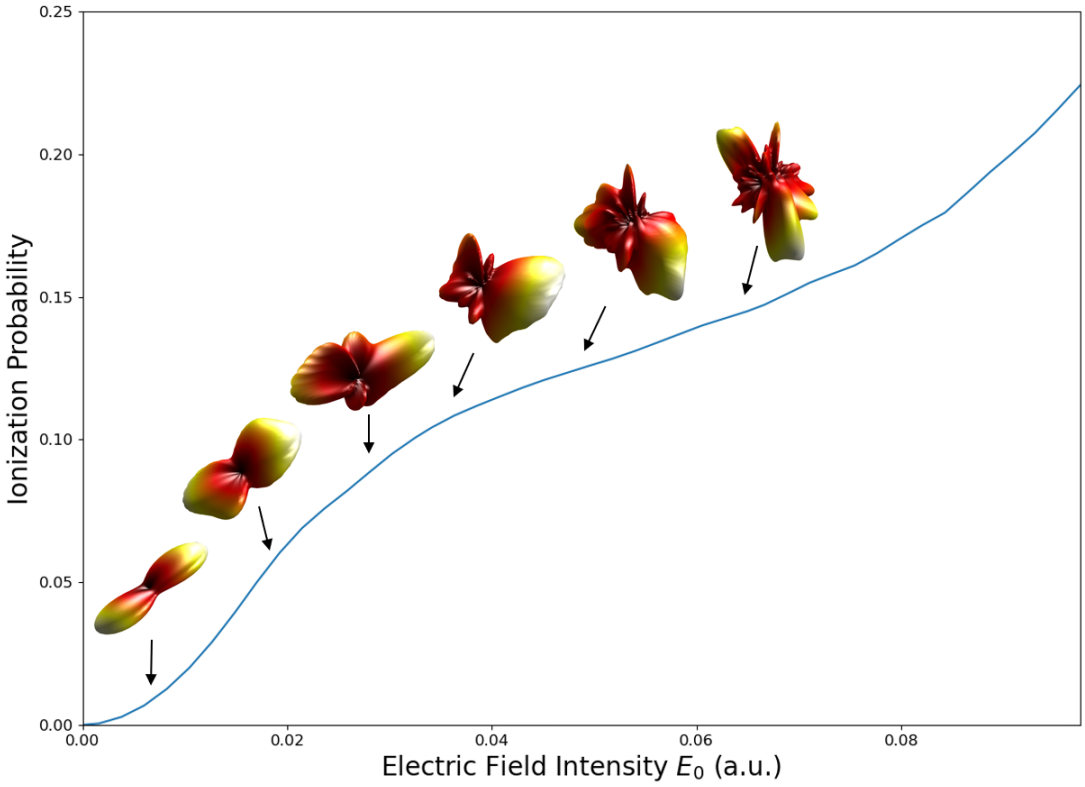

Figure 3.15: The evolution of angular distributions under an xz-polarized field, shown side by side with the corresponding ionization probability. Every distribution is depicted under the same viewing angle, so that the rotation relative to the start position would be captured.

Chapter 4

Summary and Conclusion

In this thesis, an investigation of the electron behaviour of the circular Rydberg state 5g(m=4) under the influence of circularly polarized laser fields, have been studied by solving the time-dependent Schrödinger equation numerically. Ionization probability curves originating from different field orientations in relation to the electron distribution of the 5g(m=4) state, were investigated in an intensity region below $E_0 = 0.09747$ (a.u.). Convergence tests were also performed on tuneable parameters such as the box size (r_{max}), to ensure that the results would not be significantly impacted by truncating parameters at too low values.

Ionization probability curves from a previously published article investigating co- and counter-rotating fields on the 5g(m=4) state [1], were successfully reproduced for intensities below $E_0 = 0.06498$ (a.u.). The reproduced results confirmed that the co-rotating laser-field (rotating in the same direction as the orbiting electron) produced a larger ionization yield than the counter-rotating field, and that for both field orientations *atomic stabilization* were observed in a limited intensity region. However, small structural deviations in the ionization probability curve between my results and that of the referred article, were found within a trusted intensity region for the co-rotating field.

Angular distributions were also investigated for both the counter- and co-rotating fields. The distributions from the co-rotating field produced shapes similar to the initial torus geometry of the 5g(m=4) state for small intensities, which was found to be consistent with the selection rules for single-photon absorption given in [1]. For the counter-rotating field the angular distribution had a cone-shape at low intensities, which was reasoned to be the result of a *superposition* between the two states from the single-photon transition rule; one having l=3, m=3 and the other having l=5, m=3. This hypothesis was further strengthened when the linear combination of spherical harmonics belonging to these two states, gave a very similar geometry to that of the cone-shaped angular distribution.

The evolution of angular distributions over a wider intensity range were also investigated for both the co- and counter-rotating fields, by combining them with the corresponding ionization probability into two unified figures. From these figures it was found that the co-rotating field continued to mostly produce circular angular distributions throughout the intensity sweep, while the counter-rotating field gave rise to more pillar shaped distributions.

Similar investigations to that performed on the in-plane co- and counter-rotating fields, were also conducted using a field orientation that rotated perpendicular to

the torus shaped electron distribution of the 5g(m=4) state. The perpendicular rotation resulted in significantly lower ionization yields, than that observed for the co- and counter-rotating fields. The kinetic energy distribution for this field was also investigated by plotting differential probability vs. kinetic energy for three different intensities. It was found that the differential probability curves experience a set of peaks, where each peak is separated by a single photon energy, consistent with multi-photon absorption.

4.1 Future Advancement

This study has shown that the orientation of circularly polarized laser fields have an effect on the ionization probabilities and electron angular distributions for the 5g(m=4) Rydberg state. For future work, it would be of interest to model circular states of higher l, m values, that were omitted in this thesis due to time limitations and computational restrictions. One such state could be the 10l(m=9) state, where the electron has a significantly larger orbital period. Another project could be to investigate results from using the same co- and counter-rotating fields, but having an identical rotational frequency as the orbital period of the electron. One way to do this with the 5g(m=4) electron, would be to have an eight-fold increase in the laser wavelength into the far-infrared regime, which in turn reduces the rotational frequency to approximately the orbital period.

Looking ahead, the natural application I see for Rydberg physics is in relation to quantum technologies, and especially for the development of next generation transistors and quantum-bits (q-bits). The entanglement of large q-bit arrays is one of the essential obstacles in quantum-computing, which might be overcome by Rydberg mediated interactions, as addressed in this review article [29]. Also, perhaps the *Rydberg blockade* will be a crucial effect to exploit for the production of quantum logic gates, which all ready seem to be under research [30].

Appendix A

Matrix Elements

This appendix contain the full derivation of the p_y element, and the p_x and p_z components have been included in section (2.4.1). I will frequently refer to a private document [31], where previous students and researchers (including my supervisor) have all ready derived many mathematical QM operations, and so much of the credit for this derivation should go to them. I tried to keep the same format as this document to make later comparisons easier.

A.1 p_y Element

The p_y operation to be derived can be seen in equation (A.1).

$$\langle \Psi_{k'l'm'} | \hat{p}_y | \Psi_{klm} \rangle = \langle \frac{u_{k'l'}(r)}{r} Y_{l'}^{m'}(\theta,\varphi) | - i\hbar \frac{\partial}{\partial y} | \frac{u_{kl}(r)}{r} Y_l^m(\theta,\varphi) \rangle \tag{A.1}$$

The partial derivative $\frac{\partial}{\partial y}$ contains three terms when transformed into spherical coordinates, as shown in (A.2).

$$\frac{\partial}{\partial y} = \sin(\theta)\sin(\varphi)\frac{\partial}{\partial r} + \frac{1}{r}\sin(\varphi)\cos(\theta)\frac{\partial}{\partial \theta} + \frac{1}{r}\frac{\cos(\varphi)}{\sin(\theta)}\frac{\partial}{\partial \varphi} \tag{A.2}$$

Each term in the $\frac{\partial}{\partial y}$ operation will work on Ψ_{klm}, where the spherical harmonics are defined as in (A.3).

$$\begin{aligned} Y_l^m(\theta,\varphi) &= N_l^m e^{im\varphi}\ P_l^m(cos\theta) \\ N_{lm} &= \sqrt[1]{\frac{(2l+1)(l-m)!}{4\pi(l+m)!}} \end{aligned} \tag{A.3}$$

I will now deal with each term separately, and later combine them to the full expression.

First Term: $\sin(\theta)\sin(\varphi)\frac{\partial}{\partial r}\frac{u_{kl}(r)}{r}Y_l^m(\theta,\varphi)$

The $\frac{\partial}{\partial r}$ operation on $u(r)$ will be dealt with later, so first expanding $\sin\theta$ with Euler's relation: $e^{i\varphi} = \cos\varphi + i\sin\varphi \rightarrow \sin\varphi = \frac{1}{2i}[e^{-i\varphi} - e^{i\varphi}]$ gives us (A.4).

$$\begin{aligned}\sin(\theta)\sin(\varphi)Y_l^m(\theta,\varphi) &= \frac{1}{2i}(e^{i\varphi}-e^{-i\varphi})N_l^m e^{im\varphi}\ P_l^m\sin(\theta)\\ &= \frac{1}{2i}N_l^m e^{i(m+1)\varphi}P_l^m\sin(\theta) - \frac{1}{2i}N_l^m e^{i(m-1)\varphi}P_l^m\sin(\theta)\end{aligned} \tag{A.4}$$

Now, using the relation for the Legendre polynomials in (A.5).

$$\begin{aligned}\sin\theta P_l^m &= \frac{1}{2l+1}[P_{l-1}^{m+1}-P_{l+1}^{m+1}]\\ = \frac{1}{2l+1}[(l-m+1)(l-m+2)P_{l+1}^{m-1} &- (l+m-1)(l+m)P_{l-1}^{m-1}]\end{aligned} \tag{A.5}$$

We can then select the appropriate expansion from (A.5) and combine with (A.4), leaving us with four expressions containing $P_{m\pm1}^{l\pm1}$. This will then allow us to combine $N_{(l\pm1)(m\pm1)}$ and $P_{l\pm1}^{m\pm1}$ into new spherical harmonics $Y_{l\pm1}^{m\pm1}$, doing so leads to (A.6).

$$\begin{aligned}\sin(\theta)\sin(\varphi)Y_l^m &= \frac{1}{2i}N_l^m e^{i(m+1)\varphi}\frac{1}{2l+1}[P_{l-1}^{m+1}-P_{l+1}^{m+1}]\\ -\frac{1}{2i}N_l^m e^{i(m-1)\varphi}\frac{1}{2l+1}&[(l-m+1)(l-m+2)P_{l+1}^{m-1}-(l+m-1)P_{l-1}^{m-1}]\end{aligned} \tag{A.6}$$

One of these four expressions is written out in (A.7).

$$\begin{aligned}\frac{1}{2l+1}(l-m+1)(l-m+2)N_{lm}P_{l+1}^{m-1} &=\\ \frac{(l-m+1)(l-m+2)}{\sqrt{2l+1}\sqrt{2l+3}} * &\sqrt{\frac{(2l+3)(l-m)!}{4\pi(l+m)!}}\\ = \frac{\sqrt{(l-m+1)(l-m+2)}}{\sqrt{2l+1}\sqrt{2l+3}}N_{l+1}^{m-1}P_{l+1}^{m-1} &= a_{l+1,-m+1}Y_{l+1}^{m-1}\end{aligned} \tag{A.7}$$

Where I have defined the constant a_{lm} as in (A.8), identical to what was done in the document [31].

$$a_{lm} = \sqrt{\frac{(l+m)(l+m-1)}{4(2l-1)(2l+1)}} \tag{A.8}$$

After doing this for the 4 different terms, then we get slight modifications of the constant a_{lm}. Also, when including the $(1/i)$ term, we get the following four combinations in (A.9).

$$\begin{aligned}&+\frac{1}{i}\frac{\sqrt{(l-m)(l-m-1)}}{4\sqrt{2l-1}\sqrt{2l+1}}N_{l-1}^{m+1}P_{l-1}^{m+1}\\ &-\frac{1}{i}\frac{\sqrt{(l+m+2)(l+m+1)}}{4\sqrt{2l+1}\sqrt{2l+3}}N_{l+1}^{m+1}P_{l+1}^{m+1}\\ &-\frac{1}{i}\frac{\sqrt{(l-m+2)(l+m+1)}}{4\sqrt{2l+1}\sqrt{2l+3}}N_{l+1}^{m-1}P_{l+1}^{m-1}\\ &+\frac{1}{i}\frac{\sqrt{(l+m)(l+m-1)}}{4\sqrt{2l-1}\sqrt{2l+1}}N_{l-1}^{m-1}P_{l-1}^{m-1}\\ = \underline{-i\left(a_{l,-m}Y_{l-1}^{m+1}-a_{l+1,m+1}Y_{l+1}^{m+1}-a_{l+1,-m+1}Y_{l+1}^{m-1}+a_{l,m}Y_{l-1}^{m-1}\right)}&\end{aligned} \tag{A.9}$$

This result is almost identical to the px case derived in the document [31], but there is a complex component and a change in the sign for the last two terms.

Second Term: $\frac{1}{r}\sin(\varphi)\cos(\theta)\frac{\partial}{\partial\theta}Y_l^m$

The $\frac{1}{r}$ term can be left aside, and will be multiplied back later. Also for this term we use Euler's relationship and we can express the term as in (A.10).

$$\frac{1}{r}\sin(\varphi)\cos(\theta)\frac{\partial}{\partial\theta}(Y_l^m) = \frac{1}{2i}(e^{i(m+1)\varphi} - e^{i(m-1)\varphi})N_l^m\cos\theta\frac{\partial}{\partial\theta}P_l^m \tag{A.10}$$

Using the relationship for the derivative of the Legendre polynomials, shown in (A.11).

$$\frac{\partial}{\partial\theta}P_l^m = \frac{1}{2}[P_l^{m+1} - (l+m)(l-m+1)P_l^{m-1}] \tag{A.11}$$

Replacing $\frac{\partial}{\partial\theta}P_l^m$ with this expansion, leads to (A.12).

$$\frac{1}{2i}(e^{i(m+1)\varphi} - e^{i(m-1)\varphi})N_l^m\frac{1}{2}[\cos(\theta)P_l^{m+1} - (l+m)(l-m+1)\cos(\theta)P_l^{m-1}] \tag{A.12}$$

The cosine-Legandre term can be expanded using equation (A.13).

$$\cos(\theta)P_l^m = \frac{1}{2l+1}[(l-m+1)P_{l+1}^m + (l+m)P_{l-1}^m] \tag{A.13}$$

Then we can rewrite our equation into (A.14).

$$\begin{aligned}&\frac{N_l^m}{4i}\frac{1}{2l+1}(e^{i(m+1)\varphi} - e^{i(m-1)\varphi})\times\\ &[(l-m)P_{l+1}^{m+1} + (l+m+1)P_{l-1}^{m+1}\\ -(l+m)(l-m+1)&\left((l-m+2)P_{l+1}^{m-1} - (l+m-1)P_{l+1}^{m-1}\right)]\end{aligned} \tag{A.14}$$

This leads to the final result for this term, as shown in equation (A.15), similar to that of the p_x case in the document [31].

$$\sin(\varphi)\cos(\theta)\frac{\partial}{\partial\theta}Y_l^m = \tag{A.15}$$

$$+\frac{1}{4i}N_l^m e^{i(m+1)\varphi}\frac{1}{2l+1}\left[(l-m)P_{l+1}^{m+1} + (l+m+1)P_{l-1}^{m+1}\right] \tag{A.16}$$

$$+\frac{1}{4i}N_l^m e^{i(m-1)\varphi}\frac{(l+m)(l-m+1)}{2l+1}\left[(l-m+2)P_{l+1}^{m-1} + (l+m-1)P_{l-1}^{m-1}\right]$$

$$-\frac{1}{4i}N_l^m e^{i(m-1)\varphi}\frac{1}{2l+1}\left[(l-m)P_{l+1}^{m+1} + (l+m+1)P_{l-1}^{m+1}\right]$$

$$-\frac{1}{4i}N_l^m e^{i(m+1)\varphi}\frac{(l+m)(l-m+1)}{2l+1}\left[(l-m+2)P_{l+1}^{m-1} + (l+m-1)P_{l-1}^{m-1}\right]$$

Third Term: $\frac{1}{r}\frac{\cos(\varphi)}{\sin(\theta)}\frac{\partial}{\partial\varphi}Y_l^m$

Using the Euler cosine-transformation we have (A.17).

$$\frac{\cos(\varphi)}{\sin(\theta)}\frac{\partial}{\partial\varphi}Y_l^m = \frac{im}{2}(e^{i(m+1)\varphi} + e^{i(m-1)\varphi})N_l^m\frac{P_l^m}{\sin(\theta)} \tag{A.17}$$

Rewriting this into 4 terms leads to (A.18).

$$\begin{aligned}\frac{\cos(\varphi)}{\sin(\theta)}\frac{\partial}{\partial\varphi}Y_l^m = &+\frac{im}{2}N_l^m e^{i(m+1)\varphi}\left(\frac{l-m+1}{2l+1}\frac{P_l^m}{\sin(\theta)} + \frac{l+m}{2l+1}\frac{P_l^m}{\sin(\theta)}\right)\\ &+\frac{im}{2}N_l^m e^{i(m-1)\varphi}\left(\frac{l+m+1}{2l+1}\frac{P_l^m}{\sin(\theta)} + \frac{l-m}{2l+1}\frac{P_l^m}{\sin(\theta)}\right)\end{aligned} \tag{A.18}$$

Performing another expansion of the Legendre polynomials in (A.19).

$$\begin{aligned}\frac{P_l^m}{\sin(\theta)} &= -\frac{1}{2m}[P_{l-1}^{m+1} + (l+m-1)(l+m)P_{l-1}^{m-1}]\\ &= -\frac{1}{2m}[P_{l+1}^{m+1} + (l-m+1)(l-m+2)P_{l+1}^{m-1}]\end{aligned} \tag{A.19}$$

Moving the complex "i" to the denominator changes the sign and leads to (A.20).

$$\frac{\cos(\varphi)}{\sin(\theta)}\frac{\partial}{\partial\varphi}Y_l^m = \tag{A.20}$$

$$+\frac{1}{4i}N_l^m e^{i(m+1)\varphi}\frac{1}{2l+1}\left[(l+m)P_{l+1}^{m+1} + (l-m+1)P_{l-1}^{m+1}\right] \tag{A.21}$$

$$+\frac{1}{4i}N_l^m e^{i(m-1)\varphi}\frac{1}{2l+1}\left[(l-m)(l-m+1)P_{l+1}^{m-1} + (l+m-1)(l+m)(l+m+1)P_{l-1}^{m-1}\right]$$

$$+\frac{1}{4i}N_l^m e^{i(m-1)\varphi}\frac{1}{2l+1}\left[(l-m)P_{l+1}^{m+1} + (l+m+1)P_{l-1}^{m+1}\right]$$

$$+\frac{1}{4i}N_l^m e^{i(m+1)\varphi}\frac{(l+m)(l-m+1)}{2l+1}\left[(l-m+2)P_{l+1}^{m-1} + (l+m-1)P_{l-1}^{m-1}\right]$$

These terms are very similar to the result in (A.15), and it can be noted that the last two terms have the opposite sign. Conveniently this means that the unmatched Legendre polynomials $e^{i(m\mp1)\varphi}P^{m\pm1}$ (last two terms) cancel out.

Combining Term 2+3

We will combine term 2+3 since they both contain $\frac{1}{r}$, so combining equations (A.20) and (A.15) we have (A.22).

$$+\frac{1}{2i}N_l^m e^{i(m+1)\varphi}\frac{1}{2l+1}\left[(2l)P_{l+1}^{m+1} + (2l+2)P_{l-1}^{m+1}\right] \tag{A.22}$$

$$+\frac{1}{4i}N_l^m e^{i(m-1)\varphi}\frac{1}{2l+1}\left[(l-m)(l-m+1)P_{l+1}^{m-1} + (l+m-1)(l+m)(l+m+1)P_{l-1}^{m-1}\right]$$

$$+\frac{1}{4i}N_l^m e^{i(m-1)\varphi}\frac{(l+m)(l-m+1)}{2l+1}\left[(l-m+2)P_{l+1}^{m-1} + (l+m-1)P_{l-1}^{m-1}\right]$$

Rewriting to the same format as the document leads to (A.23).

$$
\begin{aligned}
&+\frac{l}{2i}N_l^m e^{i(m+1)\varphi}\frac{1}{2l+1}P_{l+1}^{m+1} \\
&+\frac{l}{2i}N_l^m e^{i(m-1)\varphi}\frac{(l-m-1)(l-m+2)}{2l+1}P_{l+1}^{m-1} \\
&+\frac{l+1}{2i}N_l^m e^{i(m+1)\varphi}\frac{1}{2l+1}P_{l-1}^{m+1} \\
&+\frac{l+1}{2i}N_l^m e^{i(m-1)\varphi}\frac{(l+m-1)(l+m)}{2l+1}P_{l-1}^{m-1} \\
&=\underline{-i\left(la_{l+1,m+1}Y_{l+1}^{m+1}+la_{l+1,-m+1}Y_{l+1}^{m-1}+(l+1)a_{l,-m}Y_{l-1}^{m+1}+(l+1)a_{l,m}Y_{l-1}^{m-1}\right)}
\end{aligned}
\tag{A.23}
$$

Final Result

The partial derivative with respect to y in spherical coordinates can therefore be written as (A.24).

$$
\begin{aligned}
\frac{\partial}{\partial y}Y_l^m = &-i\left(a_{l,-m}Y_{l-1}^{m+1}-a_{l+1,m+1}Y_{l+1}^{m+1}-a_{l+1,-m+1}Y_{l+1}^{m-1}+a_{l,m}Y_{l-1}^{m-1}\right)\frac{\partial}{\partial r} \\
&-i\left(la_{l+1,m+1}Y_{l+1}^{m+1}+la_{l+1,-m+1}Y_{l+1}^{m-1}+(l+1)a_{l,-m}Y_{l-1}^{m+1}+(l+1)a_{l,m}Y_{l-1}^{m-1}\right)\frac{1}{r}
\end{aligned}
\tag{A.24}
$$

And when reintroducing that the derivative of $u_{kl}(r)$ as (A.25),

$$
\frac{d}{dr}\frac{u_{kl}(r)}{r}=\frac{-1}{r^2}u_{kl}+\frac{1}{r}\frac{du_{kl}}{dr} \tag{A.25}
$$

then the complete integral can be expressed as equation (A.26).

$$
\begin{aligned}
\frac{\partial}{\partial y}\left[\frac{u_{kl}(r)}{r}Y_l^m(\theta,\varphi)\right] = &-i(\frac{1}{r}\frac{du_{kl}}{dr}-\frac{l+1}{r^2}u_{kl})a_{l+1,m+1}Y_{l+1}^{m+1} \\
&-i(\frac{1}{r}\frac{du_{kl}}{dr}-\frac{l+1}{r^2}u_{kl})a_{l+1,-m+1}Y_{l+1}^{m-1} \\
&-i(\frac{1}{r}\frac{du_{kl}}{dr}+\frac{l}{r^2}u_{kl})a_{l,-m}Y_{l-1}^{m+1} \\
&-i(\frac{1}{r}\frac{du_{kl}}{dr}+\frac{l}{r^2}u_{kl})a_{l,m}Y_{l-1}^{m-1}
\end{aligned}
\tag{A.26}
$$

Inserting this into the expression for the matrix element, we have our final expression in (A.27).

$$\langle \frac{u_{kl}}{r} Y_l^m | \frac{\partial}{\partial y} | \frac{u_{k'l'}}{r} Y_{l'}^{m'} \rangle =$$
$$-ia_{l,-m}\delta_{l,l-1}\delta_{m,m+1} \int_0^{r_{max}} u_{kl} \left(\frac{du_{k',l-1}}{dr} - \frac{l}{r} u_{k',l-1} \right) dr$$
$$-ia_{l,m}\delta_{l,l-1}\delta_{m,m-1} \int_0^{r_{max}} u_{kl} \left(\frac{du_{k',l-1}}{dr} - \frac{l}{r} u_{k',l-1} \right) dr \tag{A.27}$$
$$-ia_{l+1,m+1}\delta_{l,l+1}\delta_{m,m+1} \int_0^{r_{max}} u_{kl} \left(\frac{du_{k',l+1}}{dr} + \frac{l+1}{r} u_{k',l+1} \right) dr$$
$$-ia_{l+1,-m+1}\delta_{l,l+1}\delta_{m,m-1} \int_0^{r_{max}} u_{kl} \left(\frac{du_{k',l+1}}{dr} + \frac{l+1}{r} u_{k',l+1} \right) dr$$

The p_x and p_z elements can be derived in a similar manner, however the final results for these elements are given in one of the previous sections, and can be seen in equation (2.67) and (2.66).

Appendix B

Equations

$$\psi_{nlm} = \sqrt{\left(\frac{2}{na}\right)^3 \frac{(n-l-1)!}{2n(n+l)!}} e^{-r/na} \left(\frac{2r}{na}\right)^l \left[L_{n-l-1}^{2l+1}(2r/na)\right] Y_l^m(\theta,\phi) \tag{B.1}$$

Equation from [17, p. 151].

$$Y_l^m(\theta,\varphi) = \sqrt{(\frac{(2l+1)(l-m)!}{4\pi(l+m)!})} P_l^m(cos\theta) e^{-im\varphi} = N_{lm} P_l^m e^{im\varphi} \tag{B.2}$$

Equation from [17, p. 151].

Appendix C

Calculations

C.1 Classical Time of Orbit 5g(m=4) State

The energy for a general quantum state $|nlm\rangle$ is expressed according to equation (C.1), when using atomic units.

$$E_n = \frac{-1}{2n^2} \tag{C.1}$$

The total energy of the electron (E_e), is the sum of the kinetic and potential energy. Using atomic units this becomes as in equation (C.2).

$$E_e = \frac{1}{2}v^2 - \frac{1}{r} \tag{C.2}$$

The force from the core on the electron can be expressed using the Coulomb force (F_c), and when using atomic units we have the result in equation (C.3).

$$F_c = (m_e = 1) \times a = \frac{1}{r^2} \tag{C.3}$$

This can be combined with the expression for acceleration (a) from a classical circular orbit, as in equation (C.4).

$$a = \frac{v^2}{r} = F_c = \frac{1}{r^2} \tag{C.4}$$

Substituting $n = 5$ into the energy E_n, and using that $1/r = v^2$, we have that $v = \pm\sqrt{\frac{1}{25}}$ (a.u.), as shown in (C.5).

$$\frac{-1}{2 * (25)} = \frac{1}{2}v^2 - v^2 = \frac{-1}{2}v^2 \rightarrow v = \pm\sqrt{\frac{1}{25}} \text{ (a.u.)} \tag{C.5}$$

The value for v can then be re substituted into (C.2), leading to $r = 25$ (a.u.). From here, the circumference of orbit can be estimated using $O = 2\pi r$, and classical time can be found using $t = s/v$, leading to the final answer in (C.6).

$$t = \frac{s}{v} = \frac{2\pi * 25}{1/5} = \underline{\underline{785.4}} \text{ (a.u.)} \tag{C.6}$$

Bibliography

[1] S. Askeland et al. "Stabilization of circular Rydberg atoms by circularly polarized infrared laser fields". In: *Phys. Rev. A* 84 (3 Sept. 2011), p. 033423. DOI: 10.1103/PhysRevA.84.033423. URL: https://link.aps.org/doi/10.1103/PhysRevA.84.033423.

[2] E. Tiesinga et al. "CODATA recommended values of the fundamental physical constants: 2018". In: *Rev. Mod. Phys.* 93 (2 June 2021), p. 025010. DOI: 10.1103/RevModPhys.93.025010. URL: https://link.aps.org/doi/10.1103/RevModPhys.93.025010.

[3] E. Schrödinger. "An Undulatory Theory of the Mechanics of Atoms and Molecules". In: *Phys. Rev.* 28 (6 Dec. 1926), pp. 1049–1070. DOI: 10.1103/PhysRev.28.1049. URL: https://link.aps.org/doi/10.1103/PhysRev.28.1049.

[4] J. Autschbach. "Orbitals: Some Fiction and Some Facts". In: *Journal of Chemical Education* 89.8 (2012), pp. 1032–1040. DOI: 10.1021/ed200673w. eprint: https://doi.org/10.1021/ed200673w. URL: https://doi.org/10.1021/ed200673w.

[5] T. F. Gallagher. "Rydberg atoms". In: *Reports on Progress in Physics* 51.2 (Feb. 1, 1988). Publisher: IOP Publishing, pp. 143–188. ISSN: 0034-4885. DOI: 10.1088/0034-4885/51/2/001. URL: http://dx.doi.org/10.1088/0034-4885/51/2/001.

[6] D. Kleppner. "An Introduction to Rydberg Atoms". In: *Atoms in Unusual Situations*. Ed. by Jean Pierre Briand. Boston, MA: Springer US, 1986, pp. 57–75. ISBN: 978-1-4757-9337-6. DOI: 10.1007/978-1-4757-9337-6_4. URL: https://doi.org/10.1007/978-1-4757-9337-6_4.

[7] *Special issue on Rydberg atomic physics*. 2016. URL: https://iopscience.iop.org/journal/0953-4075/page/Special_issue_on_Rydberg_atomic_physics.

[8] C. S. Adams, J. D. Pritchard, and J. P. Shaffer. "Rydberg atom quantum technologies". In: *Journal of Physics B: Atomic, Molecular and Optical Physics* 53.1 (Dec. 3, 2019). Publisher: IOP Publishing, p. 012002. ISSN: 0953-4075. DOI: 10.1088/1361-6455/ab52ef. URL: http://dx.doi.org/10.1088/1361-6455/ab52ef.

[9] D. Comparat and P. Pierre. "Dipole blockade in a cold Rydberg atomic sample [Invited]". In: *Journal of the Optical Society of America B* 27.6 (June 1, 2010). Publisher: OSA, A208–A232. DOI: 10.1364/JOSAB.27.00A208. URL: http://josab.osa.org/abstract.cfm?URI=josab-27-6-A208.

[10] J. Preclíková et al. "Unidentified transitions in one-photon intrashell dynamics in Rydberg atoms". In: *Phys. Rev. A* 85 (4 Apr. 2012), p. 043416. DOI: 10.1103/PhysRevA.85.043416. URL: https://link.aps.org/doi/10.1103/PhysRevA.85.043416.

[11] E. Oks. "Circular Rydberg states of hydrogenlike systems in collinear electric and magnetic fields of arbitrary strengths: an exact analytical classical solution". In: *The European Physical Journal D - Atomic, Molecular, Optical and Plasma Physics* 28.2 (Feb. 1, 2004), pp. 171–179. ISSN: 1434-6079. DOI: 10.1140/epjd/e2003-00308-1. URL: https://doi.org/10.1140/epjd/e2003-00308-1.

[12] E. K. Dietsche et al. "High-sensitivity magnetometry with a single atom in a superposition of two circular Rydberg states". In: *Nature Physics* 15.4 (Apr. 1, 2019), pp. 326–329. ISSN: 1745-2481. DOI: 10.1038/s41567-018-0405-4. URL: https://doi.org/10.1038/s41567-018-0405-4.

[13] T. L. Nguyen et al. "Towards Quantum Simulation with Circular Rydberg Atoms". In: *Phys. Rev. X* 8 (1 Feb. 2018), p. 011032. DOI: 10.1103/PhysRevX.8.011032. URL: https://link.aps.org/doi/10.1103/PhysRevX.8.011032.

[14] S. Haroche. "Nobel Lecture: Controlling photons in a box and exploring the quantum to classical boundary". In: *Rev. Mod. Phys.* 85 (3 July 2013), pp. 1083–1102. DOI: 10.1103/RevModPhys.85.1083. URL: https://link.aps.org/doi/10.1103/RevModPhys.85.1083.

[15] A. Waheed et al. "Suppression of multiphoton intrashell resonances in Li Rydberg atoms". In: *Phys. Rev. A* 83 (6 June 2011), p. 063421. DOI: 10.1103/PhysRevA.83.063421. URL: https://link.aps.org/doi/10.1103/PhysRevA.83.063421.

[16] D. Delande and J. C Gay. "A New Method for Producing Circular Rydberg States". In: *Europhysics Letters (EPL)* 5.4 (Feb. 1988), pp. 303–308. DOI: 10.1209/0295-5075/5/4/004. URL: https://doi.org/10.1209/0295-5075/5/4/004.

[17] Griffiths et al. *Introduction to Quantum Mechanics*. 3rd ed. Cambridge University Press, 2018. DOI: 10.1017/9781316995433.

[18] Y. Aharonov et al. "Finally making sense of the double-slit experiment". In: *Proceedings of the National Academy of Sciences* 114.25 (2017), pp. 6480–6485. ISSN: 0027-8424. DOI: 10.1073/pnas.1704649114. eprint: https://www.pnas.org/content/114/25/6480.full.pdf. URL: https://www.pnas.org/content/114/25/6480.

[19] H. Bachau et al. "Applications of B-splines in atomic and molecular physics". In: *Reports on Progress in Physics* 64.12 (Dec. 2001), pp. 1815–1943. DOI: 10.1088/0034-4885/64/12/205.

[20] Fernandes, D. Andrew, and W. R. Atchley. "Gaussian quadrature formulae for arbitrary positive measures". In: *Evolutionary bioinformatics online* 2 (Feb. 15, 2007). Publisher: Libertas Academica, pp. 251–259. ISSN: 1176-9343. PMID: 19455218. URL: https://pubmed.ncbi.nlm.nih.gov/19455218.

[21] Goswami and Debabrata. "Nobel Prize in Physics – 2018". In: *Resonance* 23.12 (Dec. 2018), pp. 1333–1341. ISSN: 0973-712X. DOI: 10.1007/s12045-018-0744-6. URL: https://doi.org/10.1007/s12045-018-0744-6.

[22] M. Müller, A. Paarmann, and R. Ernstorfer. "Femtosecond electrons probing currents and atomic structure in nanomaterials". In: *Nature Communications* 5.1 (Oct. 31, 2014), p. 5292. ISSN: 2041-1723. DOI: 10.1038/ncomms6292. URL: https://doi.org/10.1038/ncomms6292.

[23] S. Vallières et al. "Enhanced laser-driven proton acceleration using nanowire targets". In: *Scientific Reports* 11.1 (Jan. 2021), p. 2226. ISSN: 2045-2322. DOI: 10.1038/s41598-020-80392-0. URL: https://doi.org/10.1038/s41598-020-80392-0.

[24] J. C. Maxwell. "VIII. A dynamical theory of the electromagnetic field". In: *Philosophical Transactions of the Royal Society of London* 155 (1865), pp. 459–512. DOI: 10.1098/rstl.1865.0008. eprint: https://royalsocietypublishing.org/doi/pdf/10.1098/rstl.1865.0008. URL: https://royalsocietypublishing.org/doi/abs/10.1098/rstl.1865.0008.

[25] T. E. Moe and M. Førre. "Ionization of atomic hydrogen by an intense x-ray laser pulse: An ab initio study of the breakdown of the dipole approximation". In: *Phys. Rev. A* 97 (1 Jan. 2018), p. 013415. DOI: 10.1103/PhysRevA.97.013415. URL: https://link.aps.org/doi/10.1103/PhysRevA.97.013415.

[26] A. Ludwig et al. "Breakdown of the Dipole Approximation in Strong-Field Ionization". In: *Phys. Rev. Lett.* 113 (24 Dec. 2014), p. 243001. DOI: 10.1103/PhysRevLett.113.243001. URL: https://link.aps.org/doi/10.1103/PhysRevLett.113.243001.

[27] M. Førre, Simonsen, and A. Skjerlie. "Generalized velocity-gauge form of the light-matter interaction Hamiltonian beyond the dipole approximation". In: *Phys. Rev. A* 93 (1 Jan. 2016), p. 013423. DOI: 10.1103/PhysRevA.93.013423. URL: https://link.aps.org/doi/10.1103/PhysRevA.93.013423.

[28] *ACM '74: Proceedings of the Annual Association for Computing Machinery Conference*. Vol. 1. New York, NY, USA: Association for Computing Machinery, 1974. ISBN: 9781450374828. URL: https://dl.acm.org/doi/proceedings/10.1145/800182.

[29] M. Saffman. "Quantum computing with atomic qubits and Rydberg interactions: progress and challenges". In: *Journal of Physics B: Atomic, Molecular and Optical Physics* 49.20 (Oct. 2016), p. 202001. DOI: 10.1088/0953-4075/49/20/202001. URL: https://doi.org/10.1088/0953-4075/49/20/202001.

[30] K. M. Maller et al. "Rydberg-blockade controlled-not gate and entanglement in a two-dimensional array of neutral-atom qubits". In: *Phys. Rev. A* 92 (2 Aug. 2015), p. 022336. DOI: 10.1103/PhysRevA.92.022336. URL: https://link.aps.org/doi/10.1103/PhysRevA.92.022336.

[31] M. Førre. Private communication. 2021.